R-matrix analysis and prediction of low-energy neutron-induced fission cross sections for a range of Pu isotopes

O. Bouland*
CEA, DEN, DER, SPRC, Physics Studies Laboratory, Cadarache, F-13108 Saint-paul-lez-Durance, France

J. E. Lynn and P. Talou
T-2 Nuclear Theory Group, Los Alamos National Laboratory, Los Alamos, New Mexico 87545, USA
(Received 3 May 2013; published 18 November 2013)

Neutron-induced fission cross sections for the plutonium isotopes from 236 to 244 are computed for neutrons of a few keV up to 5.5 MeV incident energy, using the Hauser-Feshbach statistical theory of nuclear reactions, modified to treat the fission decay channel in the *R*-matrix formalism. The fluctuations of the fission decay widths owing to the presence of intermediate structures in the second well and to the coupling of class I and class II states are simulated by Monte Carlo sampling of the underlying model parameter distributions. The accuracy of this approach is tested relative to the results of well-known analytical formulations for the average fission cross sections. Special attention is paid to the choice and consistency of the model input parameters, in part obtained from microscopic nuclear structure calculations. The predictive capabilities offered by our method are tested against the neutron-induced fission of the very short-lived ^{243}Pu ($\tau_{1/2} = 4.95$ h) for which no measurement exist. Our calculations, consistent over all the Pu isotope series, demonstrate that ^{243}Pu is fissile, in contrast to what is reported in the standard ENDF/B-VII.1 and JEFF-3.1.2 evaluated libraries. No recommendations are made in the JENDL-4.0 data library for this isotope.

DOI: 10.1103/PhysRevC.88.054612 PACS number(s): 24.10.Pa, 24.10.Lx, 25.85.Ec

I. INTRODUCTION

An abundance of data on the neutron-induced actinide fission cross sections and higher transuranic nuclides has been built up over decades and is still being added. It is supplemented with a body of data on particle-transfer-induced fission reactions. (More recently these have often been termed *surrogate* reactions [1,2].) Yet, despite all this, the theoretical description and analysis of such reactions is still not regarded as fully satisfactory. It is our aim in this paper to show that by using the best available microscopically based reaction theory and the best available knowledge and understanding of the physics of the deformed nucleus we can calculate fission cross sections reliably enough to extract physically meaningful parameters that show consistent patterns or trends across a range of nuclides. We also aim to show that we can use this method and information to make reasonable predictions of cross sections that are unknown or poorly measured.

We limit the scope of this paper to first-chance fission, i.e., the lower neutron energy range up to about 5.5 MeV, above which inelastic neutron emission can leave the residual nucleus in a state of excitation that is high enough to give it a reasonable probability of fission. The upper limit of 5.5 MeV is also below the appearance of semidirect and direct reactions, which are not treated in this work. In the lower part of this energy range the detailed resonance structure is of great importance in determining the average fission cross section. Hence, we base the theory on an extension of the *R*-matrix theory to the fission deformation variable as outlined by Bjornholm and Lynn [3]. In the higher part of the energy range detailed resonance structure is of much less importance and the fission cross section depends largely on the level densities of the compound nucleus at barrier deformations and the level density of the target nucleus at normal deformation, which controls the competing inelastic neutron scattering reaction. Therefore, special attention is paid to modeling these level density functions and to interpreting fits to them where these are required for matching cross-section data.

Our work seeks to implement this theory using consistent sets of model input parameters for a suite of isotopes. This approach is unique in tackling the physics owing to the presence in the fission path of a secondary well. While other approaches [4–6] have been developed to cope phenomenologically with this intermediate fission structure, this paper presents a sound approach to compute consistently and to some extent predict this complex behavior of low-energy neutron-induced fission cross sections.

This article is organized as follows. The theoretical formalism is first introduced. In particular, the modifications to the Hauser-Feshbach equations needed to treat the fission channel properly are presented. Approximate formulas valid in specific situations are discussed, but an original precise Monte Carlo type calculation, involving the full sampling of the level parameters from realistic probability functions, is used when analytical approximations are not adequate. A large section of this paper is devoted to our semimicroscopic combinatorial level density calculation, the reliability of which is crucial for good agreement between measured and calculated cross sections over a large energy range. The full extent of the developments presented in this paper is now implemented in a Fortran 95 version of the AVXSF (average cross section fission) program [7]. This new code treats several types of reactions, such as neutron, particle transfer, and photon leading to fission through the same compound nucleus with a

*Corresponding author: olivier.bouland@cea.fr

single and consistent nuclear structure database. In particular, particle-transfer-induced fission data have been used in our study of even fissioning nuclei.[1] The methodology applied will be the topic of a separate publication.

The last section is devoted to the presentation of our results on the neutron-induced fission cross sections for a suite of plutonium isotopes. A consistent set of model parameters is derived, largely by fitting our theory and models to experimental data when available. The importance of fission barrier heights and barrier penetrability parameters, deformation-dependent nucleon pairing gaps, single-particle and collective excitations, and total radiative capture widths is emphasized. Our calculated fission cross sections are compared to state-of-the-art evaluated nuclear data files that are based mainly on experimental data. In addition we confirm our confidence in our model by testing the results in terms of average capture cross section for the ^{239}Pu and ^{240}Pu target isotopes relatively to the best measurements available. The paper concludes with an example of how unmeasured cross sections, in this case ^{243}Pu ($\tau_{1/2} = 4.95$ h), can be estimated with some confidence using our theory and parameters.

II. THEORETICAL BACKGROUND

A. Hauser-Feshbach theory

Neutron-induced average reaction cross-sections in the unresolved resonance and fast energy ranges, typically from a few keV to a few MeV, are commonly calculated using the Hauser-Feshbach theory [8]. The average cross section $\sigma_{cc'}$ for the entrance channel c at a given incident neutron energy E_n and exit channel c' reads

$$\sigma_{cc'}(E_n) = \sum_{J^\pi} \sigma_c^{J^\pi}(E_n) \times \sum_{s'=|I'-i'|}^{|I'+i'|} \sum_{l'=|J-s'|}^{|J+s'|} \frac{T_{c'}^{J^\pi(l's')}(E_{c'})}{\sum_{c''} T_{c''}^{J^\pi(l''s'')}(E_{c''})}, \quad (1)$$

where a channel $c \equiv (l, s)$ is defined by its relative angular momentum l and spin s and where the summations obey the usual conservation rules. I' and i' characterize the intrinsic spins of the residual nucleus and ejectile, respectively. $E_{c'}$ is the excitation energy carried by the "ejectile" in exit channel c' (and similarly for $E_{c''}$ over the various possible exit channels c''). $\sigma_c^{J^\pi}(E_n)$ is the compound nucleus formation cross section for a given (J, π), the expression of which is for neutron-induced reactions,

$$\sigma_n^{J^\pi}(E_n) = \pi \lambda\!\!\!^{-2} g_{J,I} \sum_{s=|I-\frac{1}{2}|}^{|I+\frac{1}{2}|} \sum_{l=|J-s|}^{|J+s|} T_n^{J^\pi(ls)}(E_n), \quad (2)$$

with $g_{J,I}$ representing the statistical spin factor $(2J+1)/[2(2I+1)]$ and $T_n^{J^\pi(ls)}$ representing the neutron entrance transmission coefficients.

All elastic and inelastic neutron channel transmission coefficients are calculated from the general form established by Moldauer [9],

$$T_n^{J^\pi(ls)} = 1 - \exp(-2\pi S_l), \quad (3)$$

where S_l is the neutron strength function for a given l. At the limit of small strength function, the classic narrow resonance approximation is used for capture and fission transmission coefficients,

$$T_{c'}^{J^\pi(ls)} = 2\pi \frac{\langle \Gamma_{c'} \rangle}{D_J}, \quad (4)$$

where D_J is the mean average resonance spacing for a given spin J.

To get the true average value of the reaction cross section, it is conventional to make restitution for the nonuniform resonance pattern of fluctuating widths by multiplying the Hauser-Feshbach formula [Eq. (1)] by the customary *width fluctuation correction factor* $W_{cc'}$,

$$\left\langle \frac{\Gamma_c^{J^\pi(ls)} \Gamma_{c'}^{J^\pi(l's')}}{\sum_{c''} \Gamma_{c''}^{J^\pi(l''s'')}} \right\rangle = \frac{\langle \Gamma_c^{J^\pi(ls)} \rangle \langle \Gamma_{c'}^{J^\pi(l's')} \rangle}{\sum_{c''} \langle \Gamma_{c''}^{J^\pi(l''s'')} \rangle} \times W_{cc'}. \quad (5)$$

$W_{cc'}$ is calculated by numerical integration of the general one dimension integral given by Dresner [10] (exhaustively examined by Moldauer and summarized in Eq. (42) of Ref. [9]), assuming a nonfluctuating capture width and, for other reactions, a χ^2 width distribution with ν effective degrees of freedom for n open reaction channels. Channel width fluctuations from resonance to resonance have an important effect on average cross sections. When only few channels are opened, the $W_{cc'}$ factors can significantly reduce the value of partial reaction cross sections. The exception is the elastic scattering, which is enhanced over the uniform Hauser-Feshbach estimate by up to an asymptotic factor value of three. The overall effect decreases with increasing number of channels and thus with excitation energy [11].

In the case of W_{nf}, the exit fission channel must be seen as an overall fission channel across the double-humped barrier with a corresponding effective number of degrees of freedom corrected for the intermediate structure effect. This special treatment requires additional derivations that are detailed later in this article.

B. Specialization to the double-humped barrier

Since Strutinsky [12], we know that quantum shell effects modify significantly the single-humped barrier predicted by the simple liquid-drop model and lead to a secondary well on the path to fission (schematized in Fig. 1) and two sets of compound states: the class II compound states, in which wave functions lie, by definition, predominantly in the second minimum, and the class I compound states located in the ground-state deformation well. Class I compound states have very small fission widths, $\Gamma_{\lambda_I, f}$, and are characterized by a high level density. By contrast class II compound states exhibit much larger fission widths and a much lower density at the same excitation energy. Because of the specific properties of the class II compound states and of their coupling with class I

[1] To prevent confusion between target and fissioning nuclei, the "$*$" notation is usually favored in this article for the fissioning nucleus such that ^{A}Element*.

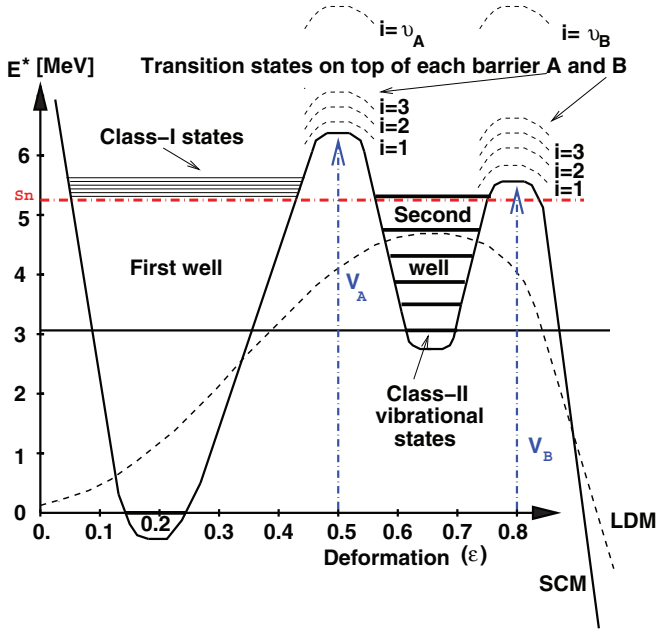

FIG. 1. (Color online) Schematic representation of the potential energy of deformation of a fissioning nucleus as a function of the elongation. Comparison is made between the single hump of the liquid drop model (LDM) and the double-hump barrier shape of the shell correction method (SCM). The macroscopic contribution provides the overall shape and magnitude of the fission barrier while microscopic corrections lead to the well-known formation of a second well along the main deformation axis.

compound states, we can eventually observe at low energy either strong resonance clusters in the resolved resonance neutron fission cross section below fission threshold [e.g., ^{240}Pu(n, f)] or large fluctuations (of average spacing $D_{\rm II}$; the class II mean level spacing) superimposed on class I-type fine structure resonances [e.g., ^{239}Pu(n, f) above neutron emission threshold]. This particular type of intermediate structure is characteristic of the presence of class II states acting as doorway states in exit fission channels.

To model the intermediate structure, the deformation variable along the fission path (symbolized by η) has been included in the R-matrix theory in an explicit and formal way by Lynn [13]. In this framework, the Hamiltonian operator is decomposed into

$$H = H_\eta + H_{\rm int}(\zeta, \eta_0) + H_c(\eta, \zeta; \eta_0), \tag{6}$$

where

(i) H_η is the sum of kinetic and potential energies of vibration in the η mode with eigenstates denoted by Φ_η;

(ii) $H_{\rm int}$, the so-called intrinsic Hamiltonian, incorporates the energies of all other degrees of freedom, denoted ζ at a fixed deformation η_0, usually set to a value corresponding to a barrier (the eigenstates of this component are denoted by χ_μ);

(iii) $H_c(\eta, \zeta; \eta_0)$ refers to the interaction between the η mode and other modes (collective- and single-particle types) of excitation.

In the presence of a double-humped fission barrier, the formal eigenstates X_λ (the observed levels in the experimental cross sections) of H [Eq. (6)] can be decomposed into two groups of auxiliary states, $X^{\rm (I)}_{\lambda_{\rm I}}$ and $X^{\rm (II)}_{\lambda_{\rm II}}$, formed from expansions on the η-vibrational states localized principally in either the primary $\Phi^{\rm (I)}_\nu$ or secondary well $\Phi^{\rm (II)}_\nu$. The resulting eigenstates X_λ are obtained from the diagonalization of H, which requires the determination of the submatrix mixing elements $\langle X^{\rm (I)}_{\lambda_{\rm I}}|H_c|X^{\rm (II)}_{\lambda_{\rm II}}\rangle$ (or the reciprocal element) characterizing the residual interaction between the $\lambda_{\rm I}$ and $\lambda_{\rm II}$ compound state sets. These elements have the following form:

$$\left\langle X^{\rm (I)}_{\lambda_{\rm I}}\middle|H_c\middle|X^{\rm (II)}_{\lambda_{\rm II}}\right\rangle \equiv \langle\lambda_{\rm I}|H_c|\lambda_{\rm II}\rangle = \sum_{\mu''\nu_{\rm II}}\sum_{\mu'\nu_{\rm I}}\langle\lambda_{\rm I}|\mu'\nu_{\rm I}\rangle\langle\mu'\nu_{\rm I}|H_c \times|\mu''\nu_{\rm II}\rangle\langle\mu''\nu_{\rm II}|\lambda_{\rm II}\rangle, \tag{7}$$

using the identity $|\mu\nu\rangle\langle\nu\mu| \equiv 1$.

$\langle\mu''\nu_{\rm II}|\lambda_{\rm II}\rangle$ is the fractionation of a class II vibrational state into the class II compound states.

Before Strutinsky and the discovery of a double-humped barrier, the importance of the coupling term H_c [Eq. (6)] was disregarded in the fission transmission coefficient calculation. In practice, it was equivalent to considering a full mixing of the deformation-intrinsic product-pair wave functions $\Phi_\nu\chi_\mu$ into the final eigenstates X_λ of H. By contrast, several cases have to be considered depending on the magnitude of the coupling strength of the class II vibrational states with the other degrees of freedom and then with the class I compound states through the $\langle\lambda_{\rm I}|H_c|\lambda_{\rm II}\rangle$ submatrix elements. An extreme situation can happen when the class II vibrational mode is not more than moderately spread into the class II compound states and, if the $\langle\lambda_{\rm I}|H_c|\lambda_{\rm II}\rangle$ elements are weak, the fission decay probability (or the fission cross section above neutron threshold energy) can exhibit the "giant" resonance characteristic of a damped vibrational resonance. This is indeed the case for the doubly even fissioning nuclei studied in this work whose fission decay probabilities were used to estimate their fission barrier heights as mentioned in the Introduction.

1. Typical coupling situations

(a) Statistical regime. In the statistical regime, it is assumed that there is a statistical equilibrium among all degrees of freedom in the compound nucleus, meaning that there is a complete mixing of the class II product-pair states in the secondary well (so-called strong damping situation). This is an assumption that manifests within the class I product-pair states because of the difference in ground-state energies between the two wells. Ultimately a full mixing arises between the two sets of compound states so that there is no more distinction between the two classes of compound states. In this framework, the fission transmission coefficient is calculated as a two-stage process [14]: Assuming a compound nucleus initially formed in an excited state of the first well and a subsequent transmission over barrier A (with transmission coefficient T_A), it can after equilibration in the second well essentially go back through the inner barrier A or fission through the outer barrier B (with transmission coefficient T_B). The effective

transmission coefficient over a specified outer Bohr fission barrier channel μ is finally

$$T_f(\mu) = \frac{T_A T_B(\mu)}{T_A + T_B + T_{\mathrm{II},\gamma} + T_{\mathrm{II},x}}, \tag{8}$$

where $T_{\mathrm{II},\gamma}$ and $T_{\mathrm{II},x}$ are, respectively, the (very small) transmission coefficients for decay of class II states by radiative and particle emission. T_A and T_B are the total fission transmission coefficients over barriers A and B calculated from the well-known Hill-Wheeler [15] expression such that

$$T_{A,B} = \sum_{J^\pi} \left[1 + \exp\left(2\pi \frac{E^{J^\pi}_{A,B} - U}{\hbar\omega^{J^\pi}_{A,B}} \right) \right]^{-1}, \tag{9}$$

with $E^{J^\pi}_{A,B}$ being the effective height corresponding to a specific J^π Bohr transition state, respectively, at saddles A and B and, U being the compound nucleus excitation energy. The sum over all J^π in Eq. (9) is unlimited because there is no genuine fission channel threshold. In practice, only a limited decisive number of channels is handled individually on top of fundamental barriers and the rest of the sum over "continuum" fission channels is approximated by an integral preserving the Hill-Wheeler tunneling shape [7] weighted by the density of the intrinsic excitation states at saddle.

Eventually, the continuum level density might be described as a series of constant-temperature regions (or phases ϕ), each characterized by their own temperature (T_ϕ), nonlinear spin-dispersion coefficient (σ_ϕ), and numerical constant (C_ϕ) such that

$$\rho_\phi(U) = C_\phi \frac{(2J+1)}{4\sigma_\phi^2} \exp \frac{\left(-J + \frac{1}{2}\right)^2}{2\sigma_\phi^2} \exp\left(U/T_\phi\right), \tag{10}$$

with $\sigma_\phi^2 = C_{1,\phi} + C_{3,\phi}\sqrt{U} + C_{2,\phi}U$.

Further considerations are made on level densities later in this article and in particular on the K quantum number dependence of Bohr fission channels.

This statistical regime is essentially reached well above the inner and outer barrier hump excitation energies or at least when the excitation energy is much larger than the peak height of the lowest hump.

(b) Sub-barrier energies: Average fission probability. At sub-barrier and near-barrier excitation energies, the detailed structure of class II levels has a significant impact on T_f. If the bulk of the strength of T_f is concentrated in a narrow energy interval about a class II level, the average fission probability will vary strongly in the vicinity of this level. In the neighborhood of a single class II level and on the assumption of uniform class I and class II level spacings (so-called "picket fence model"), Lynn and Back [16] have worked out the average fission penetrability ($\bar{P}_f$) corresponding to an intermediate structure with moderately weak class I class II coupling such that

$$\bar{P}_f = \left[1 + \left(\frac{T_\mathrm{I}}{T_f} \right)^2 + \left(\frac{2T_\mathrm{I}}{T_f} \right) \coth\left(\frac{T_A + T_B}{2} \right) \right]^{-1/2}, \tag{11}$$

with T_I being the total class I transmission coefficient including the elastic, inelastic, and radiative capture and fission open reactions within the first well.

This formula assumes a strong damping situation in the second well and does not include width fluctuation correction factors. The noncorrected average neutron-induced fission cross section, analogous to Eq. (1), is

$$\sigma_{nf}^{\text{non-cor.}} = \sum_{J^\pi} \sigma_n^{J^\pi} \bar{P}_f^{J^\pi}. \tag{12}$$

The application of Eq. (11) lowers the fission probability obtained using the statistical assumption [Eq. (8)]. It can be readily seen that Eq. (11) reduces asymptotically to $\bar{P}_f = T_F/[T_F + T_\mathrm{I}]$ in the limit of $T_A + T_B \gg 1$. However, this "*smooth-average*" fission cross section (average over many energy intervals) has to make allowance not only for the final compound nucleus state resonance width statistical fluctuations [conventionally defined by Eq. (5) and denoted W_{nf}] but also for class II coupling ($\Gamma_{\mathrm{II}\downarrow}$) and fission ($\Gamma_{\mathrm{II}\uparrow}$) width fluctuations.[2] In a first approximation, the class II width fluctuation correction factor, W_II, can be decoupled from the fission transmission coefficient calculation and reduces to the asymptotic value $W_\mathrm{II} = 2/\pi$ when the class II fission width is much greater than its coupling width. This W_II factor, approximated in such a way in a pioneer version of our AVXSF code, is now accurately calculated either by numerical integration under the same W_{nf}, W_II, and $\bar{P}_f$ decoupling hypothesis or by Monte Carlo-type simulation involving both intermediate structure and statistical width fluctuations simultaneously. Physics related to those accurate Monte Carlo calculations is summarized in the next sections.

2. Class-II state characteristics

(a) Coupling and fission widths. For a selected class II state, λ_II, the average over neighboring class I levels, λ_I, of the squared coupling matrix elements across a specified inner fission barrier channel (α), defines the concept of class II state partial coupling width, $\Gamma_{\lambda_{\mathrm{II}\downarrow}}(\alpha)$. This is summarized by the following equation:

$$\Gamma_{\lambda_{\mathrm{II}\downarrow}}(\alpha) = 2\pi \left\langle \langle \lambda_\mathrm{II} | H_c(\alpha) | \lambda_\mathrm{I} \rangle^2 \right\rangle_\mathrm{I} / D_\mathrm{I}. \tag{13}$$

By averaging over neighboring class II states, $\Gamma_{\lambda_{\mathrm{II}\downarrow}}$ can be related to the inner barrier transmission coefficient, T_A, such that

$$2\pi \left\langle \Gamma_{\lambda_{\mathrm{II}\downarrow}}(\alpha) \right\rangle_\mathrm{II} / D_\mathrm{II} = T_A(\alpha). \tag{14}$$

Similarly, the average class II fission width across a specified outer fission barrier channel μ, is related to the outer fission barrier transmission coefficient, T_B, as

$$2\pi \left\langle \Gamma_{\lambda_{\mathrm{II}\uparrow}}(\mu) \right\rangle_\mathrm{II} / D_\mathrm{II} = T_B(\mu). \tag{15}$$

To be rigorous, the fraction, $\Gamma_{\lambda_{\mathrm{II},\gamma\uparrow}}$, of the class II radiation width within the secondary well that leads to the spontaneously

[2] To prevent confusion with the "c" of channel and the "f" of the overall fission channel, Weigmann [17] notation ($\uparrow$, $\downarrow$) is favored in this article.

fissioning isomer and then to delayed fission, should be added to the class II total fission width, $\Gamma_{\lambda_{\rm II}\uparrow}$. In a neutron-induced fission cross-section framework, this correction remains very small (less than 1%).

In the present work, two main eligible intermediate structure coupling situations are considered for accurate fission cross-section Monte Carlo calculations. Both situations are discussed in Sec. II C.

(b) Width statistical fluctuations. Assuming a statistical regime, we can express the average over neighboring class II states of the double barrier fission transmission coefficient, T_f, in terms of individual class II coupling and fission widths on the basis of Eqs. (14) and (15) such that

$$\langle T_f\rangle_{\lambda_{\rm II}} \approx \left\langle \frac{T_A T_B}{T_A+T_B}\right\rangle_{\lambda_{\rm II}} = \frac{2\pi}{D_{\rm II}}\left\langle \frac{\Gamma_{\lambda_{\rm II}\downarrow}\Gamma_{\lambda_{\rm II}\uparrow}}{\Gamma_{\lambda_{\rm II}}}\right\rangle_{\lambda_{\rm II}}, \tag{16}$$

where $\Gamma_{\lambda_{\rm II}}$ represents the total width of a single class II state.

In the spirit of Eq. (5) with an expansion over the many outer barrier Bohr channels μ, we can express the right-hand side of Eq. (16) in terms of individual class II width fluctuation factor $W_{\rm II}(\mu)$ such that

$$\left\langle \frac{\Gamma_{\lambda_{\rm II}\downarrow}\Gamma_{\lambda_{\rm II}\uparrow}}{\Gamma_{\lambda_{\rm II}}}\right\rangle_{\lambda_{\rm II}} = \sum_{\mu}\left\langle \frac{\Gamma_{\lambda_{\rm II}\downarrow}\Gamma_{\lambda_{\rm II}\uparrow}(\mu)}{\Gamma_{\lambda_{\rm II}}}\right\rangle_{\lambda_{\rm II}} \tag{17}$$

$$= \sum_{\mu} W_{\rm II}(\mu)\frac{\langle\Gamma_{\lambda_{\rm II}\downarrow}\rangle\langle\Gamma_{\lambda_{\rm II}\uparrow}(\mu)\rangle}{\langle\Gamma_{\lambda_{\rm II}}\rangle}. \tag{18}$$

We now assume that the statistical fluctuations of the class II partial fission widths exhibit an independent Porter-Thomas [18] ($\nu = 1$) distribution across n fully open Bohr fission channels. If the average partial fission widths for each outer Bohr channel are equal, the distribution of the total fission widths is then ruled by a χ^2 law with $\nu = n$ degrees of freedom. A fuzzier picture is expected for the distribution across the inner Bohr fission channels, which are rather considered as a whole (i.e., as lumped channels) with no assessment on their character fully or partially open. However, the coupling width distribution, similarly to the fission width distribution, can be assumed to belong to a χ^2 family with ν, the effective value of the number of degrees of freedom.

Estimates of ν values relatively to inner and outer barriers can be extracted from first and second moments of the corresponding width distributions such that

$$\nu_{A,B} = \frac{\left[\sum_c \langle\Gamma_{\lambda_{\rm II}\downarrow,\uparrow}(c)\rangle\right]^2}{\sum_c\langle\Gamma_{\lambda_{\rm II}\downarrow,\uparrow}(c)\rangle^2} \equiv \frac{\left[\sum_c T_{A,B}(c)\right]^2}{\sum_c[T_{A,B}(c)]^2}. \tag{19}$$

Alternatively expressed in terms of transmission coefficients, estimates of $W_{\rm II}(\mu)$ are obtained by separating the fluctuating component, $T_B(\mu)$, from the constant term, $T_{B\rm cst}$, respectively associated with the individual and continuum (or lumped) outer barrier channels as

$$W_{\rm II}(\mu) = \frac{T_A + \sum_{\mu'} T_B(\mu') + T_{B\rm cst}}{T_A T_B(\mu)}\langle T_f(\mu)\rangle, \tag{20}$$

where $\langle T_f(\mu)\rangle$, the double fission barrier average transmission coefficient dedicated to an individual μ channel, is

$$\langle T_f(\mu)\rangle = \frac{\nu_A T_{B\rm cst}}{4}\left(\frac{\nu_A T_{B\rm cst}}{2T_A}\right)^{\frac{\nu_A}{2}}\prod_{\mu'}\left(\frac{T_{B\rm cst}}{2T_B(\mu')}\right)^{\frac12}\int_0^\infty dt$$
$$\times\left\{e^{-t}\left[t+\frac{\nu_A T_{B\rm cst}}{2T_A}\right]^{-(\frac{\nu_A}{2}+1)}\left[t+\frac{T_{B\rm cst}}{2T_B(\mu)}\right]^{-1}\right.$$
$$\left.\times\prod_{\mu'}\left[t+\frac{T_{B\rm cst}}{2T_B(\mu')}\right]^{-\frac12}\right\}, \tag{21}$$

while that quantity expressed for the lumped channels reduces to

$$\langle T_f(\mu)\rangle = \frac{\nu_A T_{B\rm cst}}{2}\left(\frac{\nu_A T_{B\rm cst}}{2T_A}\right)^{\frac{\nu_A}{2}}\prod_{\mu'}\left(\frac{T_{B\rm cst}}{2T_B(\mu')}\right)^{\frac12}$$
$$\times\int_0^\infty dt\,\frac{e^{-t}}{\left(t+\frac{\nu_A T_{B\rm cst}}{2T_A}\right)^{\frac{\nu_A}{2}+1}\prod_{\mu'}\left(t+\frac{T_{B\rm cst}}{2T_B(\mu')}\right)^{\frac12}}. \tag{22}$$

Equation (22) is analogous to the general single variable integral established by Dresner [10] of the $W_{n,\gamma}$ fluctuation factor. In our calculations, to speed up the processing of the $W_{n,c}$ fluctuation factors, we do consider the capture channel as a global nonfluctuative lumped channel including all constant components, meaning radiative capture, delayed fission from the second well, and fission over outer barrier continuum transition states. The very small transmission coefficient values of the highest orbital angular momentum order contributions are also mothballed in $W_{n,\gamma}$ for the same reason.

We have got now the tools to calculate the $W_{\rm II}(\mu)$ factors but we still need to estimate the effective value of the number of degrees of freedom, ν_f, corresponding to the distribution of the quasieigenstate fission widths across the double barrier, for calculating the $W_{n,f}$ factor. In standard Hauser-Feshbach statistical theory with adequate width fluctuation correction factor, ν_f should be equal to the number of open channels at the outer barrier. However, the restriction of the transmission across the outer fission channels because of the intermediate structure, acts as a reduction of ν_f. The Monte Carlo procedure, summarized in Sec. II D, supplies the frame for calculating the actual (or effective) value of ν_f. To speed up the average fission cross-section calculations, the ν_f values have been pretabulated as function of ν_A and ν_B. Each ν_f has been derived by maximum likelihood method from the value of the double barrier quasieigenstate fission width averaged over 1600 Monte Carlo trials with the assumption that, at near-barrier energy, the quasieigenstate fission width amplitude is ruled by classic broad class II state hypothesis, to be recalled in Sec. II C2.

The overall ν_f picture is presented in Fig. 2 as a bivariate plot. For comparison with classic Porter-Thomas hypothesis, the resulting values are normalized to a single fully open outer Bohr channel (i.e., ν_f is divided by ν_B). We recover the one-fission-channel single-hump situation ($\nu_f \to 1$) only when ν_A is sizable. In any other coupling situation, ν_f is

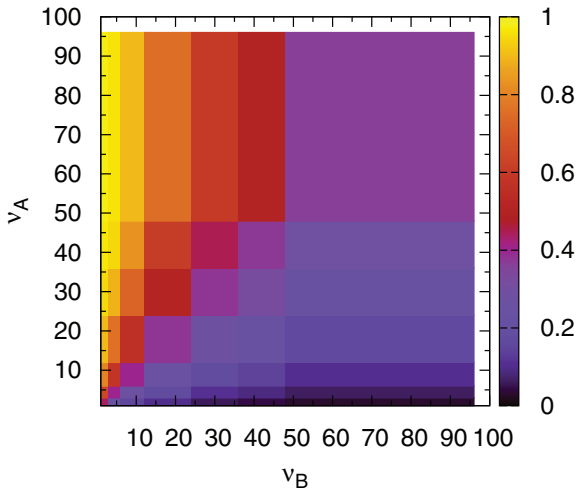

FIG. 2. (Color online) Effective number of degrees of freedom corresponding to the distribution of the quasieigenstate fission widths across the double barrier as function of ν_A (x axis) and ν_B (y axis). The resulting values are normalized to a single fully open outer Bohr channel.

strongly reduced by the intermediate structure ($0 < \nu_f < 1$) and the subsequent W_{nf} calculation will have to be corrected accordingly. In practice, this is equivalent to replacing $W_{n,f}(\nu_f^{\text{Porter-Thomas}})$ with $W_{n,f}(\nu_f^{\text{eff}})$.

(c) Level spacing distribution. Fluctuations of level spacings also impact the average cross section. However, their effect is expected to be much smaller than that of width fluctuations. The main complication that arises in introducing the level spacings is that they are not simply drawn from a frequency function but that a sequence of spacings is correlated. The long-range correlation in eigenvalue sequences is a key feature of quantum chaos [19] and is associated with the diagonalization of matrices with a large degree of randomness in their nondiagonal elements. Appendix A reviews the general problematic associated with the class I and class II level spacing distributions and, particularly, in our dedicated Monte Carlo procedure.

C. Specific class I and class II coupling modes

Monte Carlo simulations, involving actual sets of class I and class II eigenstates as described in Sec. II D, make possible the explicit treatment of class I and class II individual coupling elements. For the time being, our approach has considered only two specific sub-barrier modes that are extensively described below.

1. *Deep sub-barrier energies: Narrow class* II *(with limit arbitrarily fixed to* $\Gamma_{\lambda_{\text{II}}} \leqslant 4D_{\text{II}}$*)*

At deep sub-barrier energy, the equilibrium in the second well does not go through a simple continuum of states but rather through quasidiscrete class II states. When the class II total width, $\Gamma_{\lambda_{\text{II}}}$ (with $\Gamma_{\lambda_{\text{II}}} = \Gamma_{\lambda_{\text{II}\downarrow}} + \Gamma_{\lambda_{\text{II}\uparrow}} + \Gamma_{\lambda_{\text{II},\gamma}}$), becomes smaller than a few class I mean level spacings, we can expect very weak or moderately weak $\langle \lambda_{\text{I}_i} | H_c | \lambda_{\text{II}} \rangle$ coupling matrix elements [Eq. (8)]. Then it is legitimate to consider only a single class II state chosen at the medium energy of a sample of nearby class I states and their mixing elements.

The limitation to a single class II state (indexed 1) allows an exact diagonalization [13] of the matrix H [Eq. (6)] around this state (with energy value E_1^{II}) and the neighboring class I (with energy values E_i^{I}) to compute the eigenvalues, ε_{λ_i} ($i = 1$ to N), of the final eigenstates.

Under the two assumptions of zero mean Gaussian distribution of the $\langle \nu_{\text{I}} \alpha | H_c | \lambda_{\text{II}} \rangle$ expansion coefficients and standard normal distribution of the remaining $\langle \lambda_{\text{I}} | \nu_{\text{I}} \alpha \rangle$ expansion coefficients, the Hamiltonian matrix limited to a single class II state can be established as

$$\begin{pmatrix} E_1^{\text{II}} & \langle \lambda_{\text{II}} | H_c | \lambda_{\text{I}_1} \rangle & \cdots & \langle \lambda_{\text{II}} | H_c | \lambda_{\text{I}_{N-1}} \rangle \\ \langle \lambda_{\text{I}_1} | H_c | \lambda_{\text{II}} \rangle & E_2^{\text{I}} & \cdots & 0 \\ \cdot & \cdot & \cdots & \cdot \\ \cdot & \cdot & \cdots & \cdot \\ \langle \lambda_{\text{I}_{N-1}} | H_c | \lambda_{\text{II}} \rangle & 0 & \cdots & E_N^{\text{I}} \end{pmatrix},$$

with $(N-1)$ being the number of class I states within D_{II}.

It is convenient to express the final eigenfunctions X_λ in terms of expansion (or admixture) coefficients of class I and class II states in the diagonalized states λ_i,

$$X_{\lambda_i} = \sum_{\lambda_{\text{I}}} C_{\lambda_i(\lambda_{\text{I}})} X_{\lambda_{\text{I}}}^{(\text{I})} + C_{\lambda_i(\lambda_{\text{II}})} X_{\lambda_{\text{II}}}^{(\text{II})}, \tag{23}$$

with $C_{\lambda_i(\lambda_{\text{I}})}$ and $C_{\lambda_i(\lambda_{\text{II}})}$ directly derived from the (single class II-many class I) coupled equations such that (Eqs. (3.184) in Ref. [13])

$$\begin{aligned} C^2_{\lambda_i(\lambda_{\text{II}})} &= \left[\sum_{\lambda_{\text{I}}} \frac{\langle \lambda_{\text{I}} | H_c | \lambda_{\text{II}} \rangle^2}{\left(E_{\lambda_{\text{I}}} - \varepsilon_{\lambda_i} \right)^2} + 1 \right]^{-1} \quad \text{and} \\ C_{\lambda_i(\lambda_{\text{I}})} &= -\frac{\langle \lambda_{\text{I}} | H_c | \lambda_{\text{II}} \rangle^2}{E_{\lambda_{\text{I}}} - \varepsilon_{\lambda_i}} C_{\lambda_i(\lambda_{\text{II}})}. \end{aligned} \tag{24}$$

Note that Eqs. (23) and (24) are exact under the hypothesis of a single class II state.

In the framework of very weak or moderately weak coupling, it is plausible that a final eigenstate retains mostly the properties of the class X state (the denomination "*quasi-class X eigenstate*" will summarize this philosophy) weighted by the admixture coefficient of the latter into the final eigenstate. Eventually, if a reaction property is not exhibited by the original state, the final eigenstate might possess the missing characteristic because of the existence of, even weak, mixing matrix elements. Thus, we can comfortably assess under the classic narrow resonance approximation the following.

(i) The elastic and inelastic class I state properties reemerge in the corresponding quasiclass I eigenstate widths as

$$\Gamma_{\lambda_i(\lambda_{\text{I}}),n} = 2P_l \left[\sum_{\lambda_{\text{I}}} C_{\lambda_i(\lambda_{\text{I}})} \gamma_{\lambda_{\text{I},n}} \right]^2 \quad \text{and} \tag{25}$$

$$\Gamma_{\lambda_i(\lambda_{\text{I}}),n'} = 2P_l \left[\sum_{\lambda_{\text{I}}} C_{\lambda_i(\lambda_{\text{I}})} \gamma_{\lambda_{\text{I},n'}} \right]^2, \tag{26}$$

assuming zero mean Gaussian class I neutron elastic and inelastic *reduced*-width amplitude (respectively, $\gamma_{\lambda_{\mathrm{I},n}}$ and $\gamma_{\lambda_{\mathrm{I},n'}}$) distributions, with P_l being the neutron penetrability factor. On a similar basis but directly constructed from the average total radiative width to class I states, the total radiation width of quasi-class I eigenstates is mainly

$$\Gamma_{\lambda_i(\lambda_\mathrm{I}),\gamma} = \sum_{\lambda_\mathrm{I}} C^2_{\lambda_i(\lambda_\mathrm{I})} \bar{\Gamma}_{\lambda_\mathrm{I},\gamma}. \tag{27}$$

(ii) In the case of very weak coupling the quasi-class II eigenstate neutron elastic width is negligible because of the second-well origin, whereas the quasi-class II total radiation width can retain at least the radiative strength of the original class II and is calculated on the same footing as $\Gamma_{\lambda_i(\lambda_\mathrm{I}),\gamma}$:

$$\Gamma_{\lambda_i(\lambda_\mathrm{II}),\gamma} = C^2_{\lambda_i(\lambda_\mathrm{II})} \bar{\Gamma}_{\lambda_\mathrm{II},\gamma}. \tag{28}$$

(iii) In the end, the outer barrier partial fission widths, $\Gamma_{\lambda_i,f}(\mu)$, of a final eigenstate arise from the spreading of the subsequent class II state fission strength and are directly calculated as

$$\begin{aligned}\Gamma_{\lambda_i(\lambda_\mathrm{I}\text{ or }\lambda_\mathrm{II}),f}(\mu) &= \gamma^2_{\lambda_i,f}(\mu) \\ &= \left[C_{\lambda_i(\lambda_\mathrm{II})}\gamma_{\lambda_\mathrm{II}\uparrow}(\mu)\right]^2,\end{aligned} \tag{29}$$

on the assumption of zero mean Gaussian $\gamma_{\lambda_\mathrm{II}\uparrow}(\mu)$ partial fission width amplitude distribution with $\bar{\Gamma}_{\lambda_\mathrm{II}\uparrow}(\mu)$ standard deviation value.

2. *Sub-barrier energies: Broad class* II *state* ($\Gamma_{\lambda_\mathrm{II}} > 4D_\mathrm{I}$)

In the situation where the class II total width becomes larger and its strength spreads through its coupling width over many class I states ($\Gamma_{\lambda_\mathrm{II}\downarrow} \gg \Gamma_{\lambda_\mathrm{II}\uparrow}$), the mixing elements are somewhat large (so-called moderately weak coupling) and the class II state fission width is mixed in a Lorentzian pattern into the final *R*-matrix states. A similar resonance pattern is observed when the class II state strength is spread by its fission width instead (weak coupling situation). However, the real-type level parameters of *R*-matrix formulation no longer represent directly the widths of the observed resonances in the cross section. This weak coupling situation requires the expansion of the collision matrix (denoted *S* and derived from the *R* matrix [3]) form of the collision matrix in the complex energy plane to find the various *S*-matrix poles and, in particular, the very broad complex pole (Ref. [17], pp. 82–84). To deal with both cases, the exhaustive complex pole formulation can be adopted to calculate the resulting fission widths in terms of absolute values of the residues. Owing to the rather large class I state sample overlapped, mixing element contributions from neighboring class II states have to be considered as well and are calculated using the detailed approach just mentioned. The major contribution to final eigenstate widths is, however, calculated very simply from average class I and class II properties and suitable class II coupling width.

We postulate from the properties of the two extreme situations ($\Gamma_{\lambda_\mathrm{II}\downarrow} \gg \Gamma_{\lambda_\mathrm{II}\uparrow}$ or $\Gamma_{\lambda_\mathrm{II}\downarrow} \ll \Gamma_{\lambda_\mathrm{II}\uparrow}$), that the fission width amplitude of the quasi-class II state (which is originally the class II state located at the median energy in the class I compound state sample) can be estimated as follows

$$\gamma_{\lambda_i(\lambda_\mathrm{II}),f}(\mu) = \sqrt{1 - \frac{\Gamma_{\lambda_\mathrm{II}\downarrow}}{\Gamma_{\lambda_\mathrm{II}}}}\,\gamma_{\lambda_\mathrm{II}\uparrow}(\mu). \tag{30}$$

On a similar ground, we address the associated radiative capture width, gathering both first- and second-well radiative capture decay contributions:

$$\Gamma_{\lambda_i(\lambda_\mathrm{II}),\gamma} = \left(1 - \frac{\Gamma_{\lambda_\mathrm{II}\downarrow}}{\Gamma_{\lambda_\mathrm{II}}}\right)\bar{\Gamma}_{\lambda_\mathrm{II},\gamma} + \frac{\Gamma_{\lambda_\mathrm{II}\downarrow}}{\Gamma_{\lambda_\mathrm{II}}}\bar{\Gamma}_{\lambda_\mathrm{I},\gamma}. \tag{31}$$

Associated elastic and inelastic neutron widths exhibit the first-well properties carried into the quasi-class II eigenstate,

$$\Gamma_{\lambda_i(\lambda_\mathrm{II}),n} = \frac{\Gamma_{\lambda_\mathrm{II}\downarrow}}{\Gamma_{\lambda_\mathrm{II}}}\bar{\Gamma}_{\lambda_\mathrm{I},n} \quad \text{and} \tag{32}$$

$$\Gamma_{\lambda_i(\lambda_\mathrm{II}),n'} = \frac{\Gamma_{\lambda_\mathrm{II}\downarrow}}{\Gamma_{\lambda_\mathrm{II}}}\bar{\Gamma}_{\lambda_\mathrm{I},n'}, \tag{33}$$

with $\bar{\Gamma}_{\lambda_{\mathrm{I},n}}$ and $\bar{\Gamma}_{\lambda_{\mathrm{I},n'}}$ the average class I elastic and inelastic neutron widths. The corresponding quasi-class I widths are accordingly established as

$$\Gamma_{\lambda_i(\lambda_\mathrm{I}),n} = \Gamma_{\lambda_\mathrm{I},n} \quad \text{and} \quad \Gamma_{\lambda_i(\lambda_\mathrm{I}),n'} = \Gamma_{\lambda_\mathrm{I},n'}. \tag{34}$$

Quasi-class I eigenstate capture widths carry principally the electromagnetic radiation width of first well and are approximatively equal to the average class I capture width

$$\Gamma_{\lambda_i(\lambda_\mathrm{I}),\gamma} \approx \bar{\Gamma}_{\lambda_\mathrm{I},\gamma}. \tag{35}$$

In addition to the main second-well capture decay contribution [first term of the right-hand side of Eq. (31)] from the medium-energy class II compound state, we might consider the capture terms from neighboring class II states ($\lambda^{\mathrm{nbg.}}_\mathrm{II}$) acting as second-order effects on quasi-class I eigenstate capture widths. So we postulate that

$$\Gamma_{\lambda_i(\lambda_\mathrm{I}),\gamma} = \bar{\Gamma}_{\lambda_\mathrm{I},\gamma} + \sum_{\lambda^{\mathrm{nbg.}}_\mathrm{II}} \frac{\langle\lambda_\mathrm{I}|H_c|\lambda_\mathrm{II}\rangle^2 \cdot \bar{\Gamma}_{\lambda_\mathrm{II},\gamma}}{\left(E_{\lambda_\mathrm{II}} - \varepsilon_{\lambda_i}\right)^2 + \Gamma^2_{\lambda_\mathrm{II}}/4}. \tag{36}$$

In our current version of AVXSF, we include the fission decay from quasi-class I eigenstates owing to neighboring class II state contributions. These are assessed in terms of complex *S*-matrix poles with an additional expansion over the inner barrier channels (α). Thus, we set

$$\gamma_{\lambda_i(\lambda_\mathrm{I}),f}(\mu) = \sum_\alpha \sum_{\lambda^{\mathrm{nbg.}}_\mathrm{II}} \frac{\langle\lambda_\mathrm{I}|\alpha\rangle\langle\alpha|H_c(\mu)|\lambda_\mathrm{II}\rangle\gamma_{\lambda_\mathrm{II}\uparrow}(\mu)}{\left(E_{\lambda_\mathrm{II}} - \varepsilon_{\lambda_i}\right) - i\Gamma_{\lambda_\mathrm{II}}/2}. \tag{37}$$

Because the broadness of the class II state width can decouple significantly the mixing of class I and class II states, we assume that the eigenstate energies are only slightly perturbed, and so

$$\begin{aligned}\varepsilon_{\lambda_i(\lambda_\mathrm{I})} &\approx E_{\lambda_\mathrm{I}} \quad \text{for the quasi-class I states and} \\ \varepsilon_{\lambda_i(\lambda_\mathrm{II})} &\approx E_{\lambda_\mathrm{II}} \quad \text{for the quasi-class II state.}\end{aligned} \tag{38}$$

From a rigorous point of view, the above calculations of the formal R-matrix fission width amplitudes have to include also the contribution of the most distant class II compound states acting as a third-order effect. Appendix B reports the relevant equations.

D. Direct Monte Carlo sampling of class I and class II state parameters for R-matrix calculations

An efficient alternative to analytical expressions valid only under specific conditions, such as the statistical regime (Sec. IIB1a), the moderately weak coupling (Sec. IIB1b), or even the very weak coupling formulation described in Ref. [3], is the Monte Carlo method. The Monte Carlo procedure presents the advantage of providing average cross sections taking full account of statistical nuclear data parameter fluctuations under the relevant intermediate structure coupling condition. Our present approach simulates R-matrix resonance properties of a selected class II state and those of the overlapped neighboring class I states, over at least a full class II energy spacing, using a chain of pseudorandom numbers for a fine-tuned selection process based on both level width and spacing statistical distributions with suitable averages. To model the full extent of intermediate structure fluctuations, the Porter-Thomas width distributions of the dedicated elements $[\langle\lambda_{\rm I}|H_c|\lambda_{\rm II}\rangle^2$, $\Gamma_{\lambda_{\rm II}\downarrow}$, and $\Gamma_{\lambda_{\rm II}\uparrow}$, as introduced by Eqs. (13)–(15), respectively] were simulated accordingly.

In this work, the accurate Monte Carlo procedure was carried each time as possible and in most cases supersedes the analytical route and that, especially at deep sub-barrier excitation energies (very weak coupling situation) where the Lynn and Back formula fails. In this context, the average fission cross section is directly retrieved as

$$\sigma_{nf}(E_n) = \sum_{J^\pi} \sigma_n^{J^\pi}(E_n) \times \sum_{s'=|I'-i'|}^{|I'+i'|} \sum_{l'=|J-s'|}^{|J+s'|} \bar{P}_{f,\rm MC}^{J^\pi(l's')}, \qquad (39)$$

with $\bar{P}_{f,\rm MC}^{J^\pi(l's')}$ the exact average fission probability for given (J,π) computed by direct Monte Carlo treatment and $\sigma_n^{J^\pi}(E_n)$ the neutron-incident compound nucleus formation cross section for given (J,π) defined by Eq. (2).

At this stage, it is appropriate to get a feeling for the various ingredients involved in the calculation of $\bar{P}_{f,\rm MC}$ by making reference to the classic decoupling hypothesis between the average fission sub-barrier probability $\bar{P}_f$ and the $W_{n,c}$ and $W_{\rm II}$ fluctuation correction factors. In this perspective and on the argumentation developed in Sec. IIB2b, $\bar{P}_{f,\rm MC}$ can be pictured as

$$\bar{P}_{f,\rm MC} \equiv W_{nf}\left(\nu_f^{\rm eff}\right) \times \bar{P}_f \times W_{\rm II}. \qquad (40)$$

Figures 3 and 4 show the behavior of the right-hand-side terms of Eq. (40) as a function of neutron-incident energy, respectively, for the ^{239}Pu fissile and ^{240}Pu nonfissile target isotopes. We verify that both the typical sub-barrier tunneling effect [estimated from the ratio of the Lynn and Back formula—Eq. (11)—to the statistical regime—Eq. (8)] and the overall width statistical fluctuation correction [estimated from the $W_{nf}(\nu_f^{\rm eff}) \times W_{\rm II}$ product] strongly impact the average fission cross-section magnitude. Depending on fission barrier heights relatively to neutron threshold energy, the sub-barrier tunneling effect is either much smaller than the overall statistical width fluctuation correction (typical situation of fissile target isotopes as visible on Fig. 3) or much larger in the case of nonfissile target nuclides (Fig. 4).

Fluctuation calculations have been carried up to a maximum excitation energy of 2.1 MeV above the neutron binding energy in the present study. Figures 3 and 4 well consolidate the choice of this upper limit.

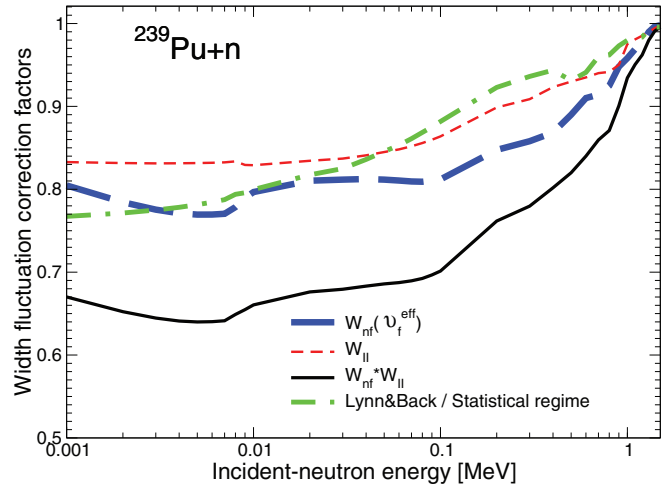

FIG. 3. (Color online) $W_{nf}(\nu_f^{\rm eff})$, $W_{\rm II}$, and $W_{nf}(\nu_f^{\rm eff}) \times W_{\rm II}$ width fluctuation correction factors calculated versus energy for the ^{239}Pu + n reaction. The average correction for the sub-barrier tunneling effect (green double-dash-dotted curve) is similar to both the $W_{nf}(\nu_f^{\rm eff})$ (blue long-dashed curve) and $W_{\rm II}$ (red short-dashed curve) corrections and so significantly smaller than the correction owing to the overall fluctuations [$W_{nf}(\nu_f^{\rm eff}) \times W_{\rm II}$ product; black solid line].

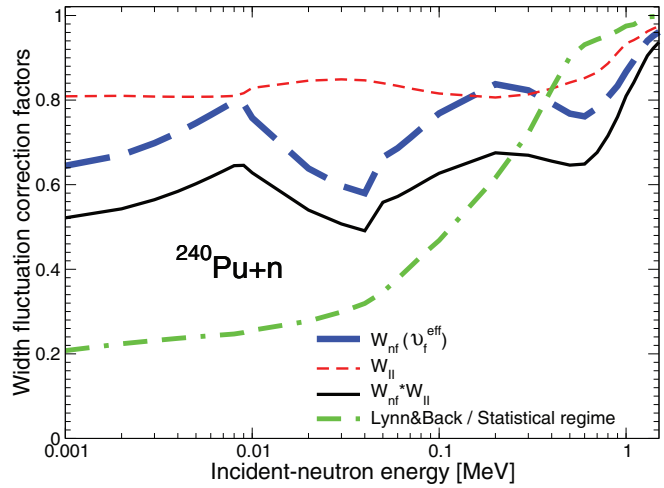

FIG. 4. (Color online) $W_{nf}(\nu_f^{\rm eff})$, $W_{\rm II}$, and $W_{nf}(\nu_f^{\rm eff}) \times W_{\rm II}$ width fluctuation correction factors calculated for the ^{240}Pu + n reaction. The average correction for the sub-barrier tunneling effect (green double-dash-dotted curve) is significantly larger than the correction owing to the overall fluctuations [$W_{nf}(\nu_f^{\rm eff}) \times W_{\rm II}$ product; black solid line], as expected for manifest cases of subthreshold fission.

III. COMBINATORIAL QUASI-PARTICLE-VIBRATIONAL-ROTATIONAL LEVEL DENSITY CALCULATION

Models of the level density vary from semiempirical approaches such as the composite prescription of Gilbert and Cameron [20] to fully microscopic techniques with pairing correlations, vibrations, and rotational excitations calculated for each many-particle-many-hole excited state (such as Ref. [21]). Although the former are well suited for practical fits on available experimental data, we might expect that the latter possess more predictive capabilities outside the fitting region because they are based on realistic single-particle spectrum calculations. They also allow us to deal, with some confidence, with level densities for larger deformations for which there is no direct experimental evidence. The method developed in this article aims to combine both virtues by associating microscopic- and macroscopic-type information.

(i) The microscopic-type information reposes on the poles of the quasiparticle Tamm-Dancoff approximation [22] secular equation which supplies the unperturbed one-quasiparticle excitations on the many-body configuration,

$$E_\nu^{\rm exc} = \sqrt{(e_\nu - \lambda)^2 + \Delta^2}, \tag{41}$$

with e_ν, being the energy of the single-particle state ν and, λ and Δ, respectively the Fermi energy and pairing gap with differentiation between neutron and proton. Detailed microscopic information is obtained from a neutron and proton single-particle Nilsson state data base currently set up from Ref. [23].

(ii) The macroscopic-type information is contained in the present vibrational treatment, which relies directly neither on formal calculations of phonon vibrational excitation energies nor on empirical vibrational enhancement factor. We favored instead fined-tuned vibrational spectra information from experimental measurement feedback or from collective shell models with excitation of few or many nucleons leading to near-spherical or permanent prolate-spheroid deformations [24]. In the case of an even-even fissioning nucleus, the lowest part of the spectrum is sparsely populated with levels of only collective character because the lowest quasiparticle states resulting from the breaking of a neutron or a proton pair demand a minimum energy equal to $2\Delta_n$ or $2\Delta_p$, respectively, as suggested by Eq. (41).

The strategy adopted consists of constructing the relevant vibrational spectrum from the zero-vibration ground-state energy and the four elementary quanta which describe, respectively,

(i) the β_2 vibration about the prolate equilibrium shape (cylindrical symmetry axis) [this degree of freedom will act as the overall fission variable of Eq. (6) (i.e., $\eta \equiv \beta_2$) and therefore will not be present in the Bohr transition spectrum, whereas it will show up in the inelastic spectrum];

TABLE I. Nonexhaustive phonon spectrum of collective character expected on top of the inner fundamental barrier of the ^{241}Pu fissioning nucleus. Resulting multiphonon state energies can deviate from the rule given by Eq. (42) because of anharmonicity effect in the dedicated oscillator potential.

Vibrational state	Energy (MeV)	Spin projection ($\hbar$)	Parity
Zero-vibration ground state	0.00	2.5	+1
1 γ phonon	0.14	2	+1
2 γ phonons	0.41	0	+1
2 γ phonons	0.35	4	+1
3 γ phonons	0.56	2	+1
3 γ phonons	0.48	6	+1
1 α_3 phonon	0.70	0	−1
1 $\alpha_3 + 1$ γ phonon	0.84	2	−1
1 $\alpha_3 + 2$ γ phonons	1.05	4	−1
1 $\alpha_3 + 3$ γ phonons	1.15	0	−1
1 bending phonon	0.80	1	−1
1 bending + 1 γ phonon	0.94	1	−1
1 bending + 1 γ phonon	0.94	3	−1

(ii) the γ vibration, in the two directions perpendicular to the β_2 axis, which describes the departure from spheroidal symmetry (so-called axial asymmetry),

(iii) the mass asymmetry octuple vibration (so-called α_3), which attests any softness towards pear-shape oscillations across the reflection plane,

(iv) and finally a higher order octuple vibration known as *bending* vibration.

Those β_2, γ, α_3, and bending elementary quanta are then combined together to build multiphonon collective states (a nonexhaustive sketch of those for the ^{241}Pu* fissioning nucleus is presented on Table I), for which energies (E), spin projections on the β_2 axis (K), and parities (π) follow the rules below:

$$\begin{aligned} E_{\text{multi-vib}} &= \sum_{\text{vib}=1}^{N} E_{\text{vib}}, \\ K_{\text{multi-vib}} &= \left| K_{\text{vib}_1} \pm K_{\text{vib}_2} \pm \cdots \pm K_{\text{vib}_N} \right|, \\ \pi_{\text{multi-vib}} &= \prod_{\text{vib}=1,N} \pi_{\text{vib}}. \end{aligned} \tag{42}$$

In the case of an even-N-odd-Z fissioning nucleus, the lowest excited states are, on the contrary, constructed from a single-quasiproton state (or, for an odd-odd nucleus, a two-quasiparticle state made from one single-quasineutron and one single-quasiproton) carrying vibrational states and subsequent rotational states. The energy, $E_{\rm rot}$, of each rotational state is established classically relative to the fundamental barrier height, V_f, and parity, K, of the bandhead such that

$$E_{\rm rot} = \{\hbar^2/(2\Im)\}\{J(J+1) - K(K+1)\} + V_f, \tag{43}$$

with

$$J^\pi = \begin{cases} K^\pi, (K+1)^\pi, (K+2)^\pi, \ldots & \text{for} \quad K \neq 0, \\ 0^+, 2^+, 4^+, \ldots & \text{for} \quad K = 0^+, \\ 1^-, 3^-, 5^-, \ldots & \text{for} \quad K = 0^-, \end{cases}$$

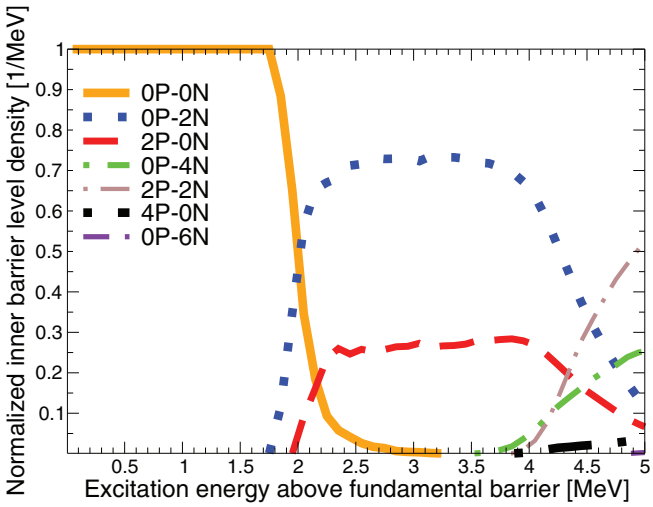

FIG. 5. (Color online) Simulated normalized combinatorial quasiparticle-vibrational-rotational LD versus excitation energy above the inner barrier fundamental height of the ^{240}Pu even-even fissioning system. The various quasiparticle contributions with aZ protons and bN neutrons are well dissociated. At low excitation energy (below $2\Delta_n$ and $2\Delta_p$; i.e., 1.75 MeV for ^{240}Pu) the LD of an even-even CN is built solely from pure collective excitations (configuration $0Z$-$0N$).

where $\hbar^2/(2\Im)$ is the rotational band constant and $\Im$ is the effective moment of inertia and is deformation dependent. However, only the excitation states of purely collective character are regulated by those rules when $K = 0$ because of the dissimilar nature of the quasiparticles which are not constrained by the reflection symmetry condition.

Above the breaking of a neutron- or a proton-pair energy, multi-quasiparticle states carrying multiphonon vibrational states show up in the even-even fissioning nucleus spectrum. These multi-quasiparticle configurations are built according to Eq. (42) and are labeled by the numbers of free protons (aZ) and neutrons (bN) such that we expect the gradual appearance of $0Z-2N, 2Z-0N, 0Z-4N, 2Z-2N$, etc., or $1Z-3N$, $3Z-1N$, $1Z-5N$, $3Z-3N$, etc., respectively, for an even-N-even-Z or odd-N-odd-Z fissioning nucleus. The various energy thresholds are well visible in Fig. 5. We realize immediately that low excitation energy level density (LD) slopes and magnitudes are very sensitive to the presence or not of quasiparticles states right above the ground state, as Fig. 6 shows. Missed LD quasiparticle contributions might cause severe difficulties for fission cross-section fits of odd-odd fissioning nuclei.

IV. ESTIMATED PARAMETER VALUES

A. Fission barrier heights

The present work using the well-known Hill and Wheeler [15] transmission coefficient definition is based on two common approximations: a unique one-dimensional fission path and a representation of fission barriers as inverted parabola.

The approximation of a unique one-dimensional fission path appears well justified in the case of plutonium isotopes,

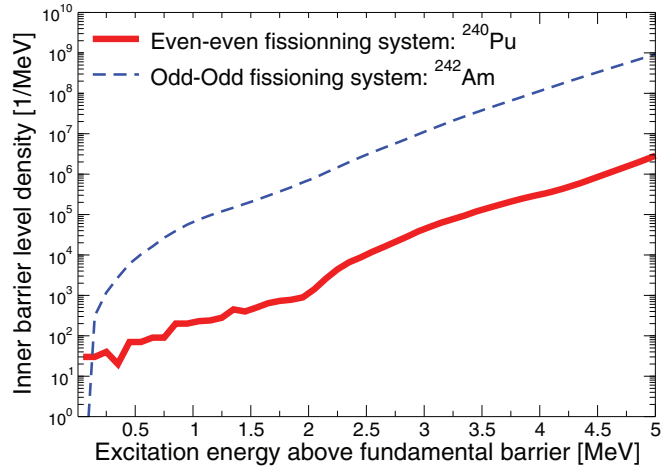

FIG. 6. (Color online) Comparison of simulated combinatorial quasiparticle-vibrational-rotational level densities between an even-even (^{240}Pu, thick solid curve) and an odd-odd compound nucleus (^{242}Am, thin dotted curve) in terms of slope and magnitude.

as predicted by the static finite range liquid drop model (FRLDM) calculations of Möller *et al.* [25]. The asymmetric mode remains the main contribution to fission until past the outer saddle point from which the symmetric path becomes relevant. Even when these two modes coexist, they remain distinct because of the existence of a significant separating ridge (at least 1 MeV above the upper valley).

Figure 7 brings also a piece of information about the validity of the inverted parabola approximation. This latter assumption clearly appears to be well justified only for the heaviest isotopes of plutonium (above mass 241). Further work will be needed to explore the influence of replacing parabolic fission barriers by more realistic shapes taken directly from nuclear structure calculations such as FRLDM or Hartree-Fock.

Impact of the triaxiality observed at the inner barrier (see Table XI of Ref. [26]) is taken into account in our calculations

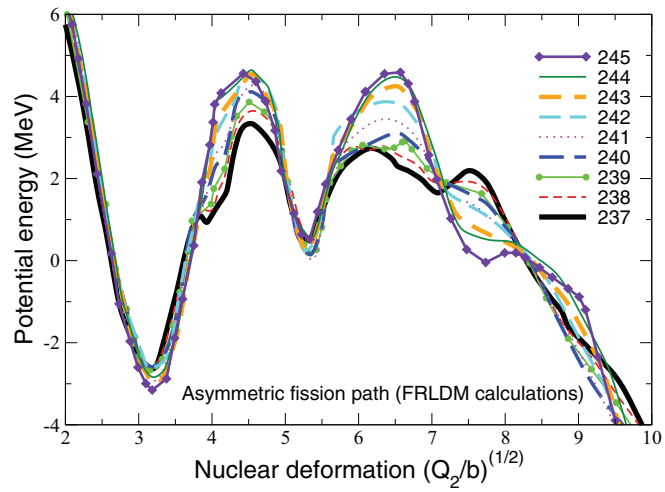

FIG. 7. (Color online) Fission paths—asymmetric mode displayed only—obtained in static FRLDM calculations by Möller *et al.* [31] for the plutonium series as a function of the elongation (with Q_2/b, the normalized charge quadrupole moment).

TABLE II. Fission barrier parameters selected in this work for Pu isotope cross section modeling. Neutron emission threshold (S_n) values are displayed for enlightening the fissile or fertile nature of each isotope.

Fissioning Pu isotope mass number	V_A (MeV)	$\hbar\omega_A$ (MeV)	V_B (MeV)	$\hbar\omega_B$ (MeV)	S_n (MeV)
237	5.60	0.99	4.95	0.40	5.86
238	5.65	1.05	5.45	0.60	7.00
239	6.05	0.98	5.55	0.55	5.65
240	5.65	1.05	5.23	0.60	6.53
241	5.91	0.95	5.67	0.60	5.24
242	5.40	1.05	5.30	0.60	6.31
243	5.83	0.85	5.48	0.50	5.03
244	5.30	1.05	5.25	0.60	6.02
245	5.56	0.83	5.17	0.48	4.72

by modulating, for instance, the circular frequency associated to the γ axis primary phonon vibration excitation. Whenever the axial symmetry is recovered (at the outer barrier for instance), the softness towards this axis is released by supplying a high phonon quantum value. Barrier parameters are usually derived from experimental observations and theoretical assessments. Table II displays our consistent set of evaluated fission barrier parameters, while Figs. 8 and 9 compare barrier heights obtained with those supplied by Bjørnholm and Lynn [3], Möller *et al.* [25], and alternatively compiled in the RIPL-3 database [26]. This latter supplies two distinct sets of fission barrier heights, one determined empirically by Maslov *et al.* [27] from experimental fission cross section data near threshold and another one based on Hartree-Fock-Bogolyubov (HFB) calculations by Goriely *et al.* [28]. A few comments can be made from these figures. The overview of our results (red line) shows a general agreement with empirical data found in the literature. However, the agreement with theoretical

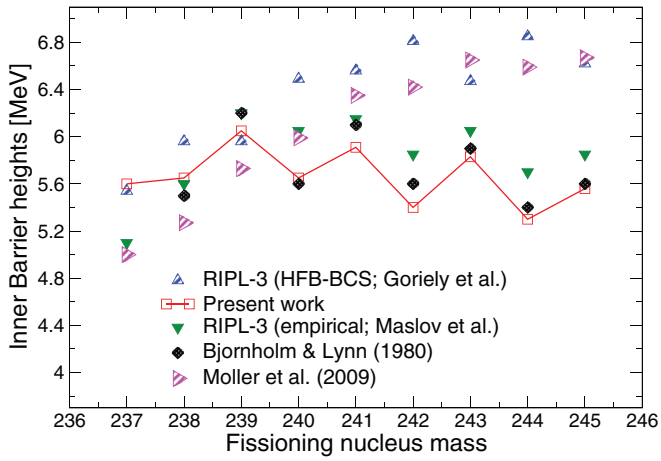

FIG. 8. (Color online) Systematics of Pu inner fission barrier heights extracted from the present work and compared with previous estimations from Bjørnholm and Lynn [3], theoretical calculations by Möller *et al.* [25] and Goriely *et al.* [28], and the empirical values reported in the RIPL-3 database [26].

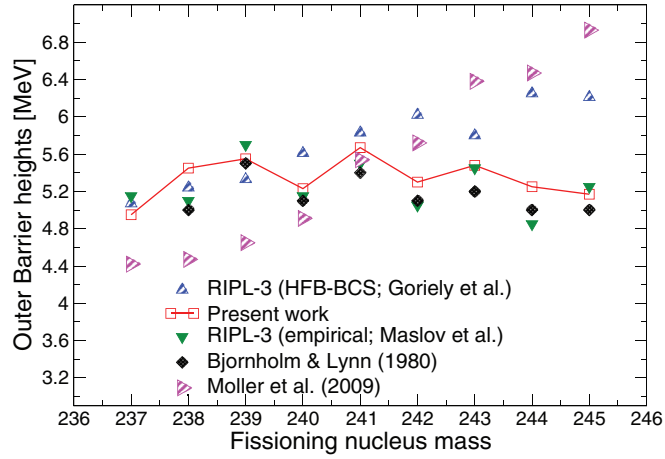

FIG. 9. (Color online) Same as Fig. 8 but for the Pu outer fission barrier heights.

predictions (FRLDM [25], right-pointing triangles; or HFB-BCS [28], up-poining triangles) is poor.

The results from both microscopic [28] and macro-microcopic [25] calculations increase smoothly with mass number, whereas our barrier heights reveal an odd-even character. The so-called "empirical" heights extracted by Maslov [27] (down-pointing triangles) are logically more consistent with our results. Data from Ref. [3] have been used as prior inputs for the present work. Prior $\hbar\omega_{A,B}$ values can be obtained from detailed resonance parameter analyses of experimentally resolved class II state clusters. A pertinent example of fine resonance structure study is the analysis made by Auchampaugh and Weston [29], who were able to extract the values[3] of $0.71^{+0.21}_{-0.09}$ MeV and $0.53^{+0.09}_{-0.06}$, respectively, for the $(V_A - S_n)/\hbar\omega_A$ and $(V_B - S_n)/\hbar\omega_B$ ratios corresponding to the system $^{240}\mathrm{Pu} + n$ (i.e., $\hbar\omega_A = 1.06$ MeV and $\hbar\omega_B = 0.81$ MeV relative to present barrier heights). However, we recall that no special provision has been made in the present work to reproduce observed fluctuations in the unresolved resonance energy range, as for instance by putting explicitly vibrational resonances in our calculation. Possible spin dependence of the barrier heights can be estimated from fission cross-section fits at high energies (above 100 keV), involving mainly higher order l-wave components, which suggest, for instance, as plausible curvature values for the ^{241}Pu fissioning nucleus: $\hbar\omega_A^{J=1/2} = 0.95$, $\hbar\omega_A^{J=3/2} = 0.83$, and $\hbar\omega_A^{J=5/2} = 0.74$ and $\hbar\omega_B^{J=1/2} = 0.60$, $\hbar\omega_B^{J=3/2} = 0.54$, and $\hbar\omega_B^{J=5/2} = 0.46$.

In terms of barrier heights, we cannot expect usually an uncertainty smaller than 200 keV because barrier heights and transition state level densities play an anticorrelated role resulting in several possible combinations of input parameters with similar degrees of confidence. In the case of fissile target isotopes, we overcome the difficulty of estimating barrier heights below the neutron separation energy with the insertion of transfer reaction data in the experimental database. Transfer reaction data analyses, performed consistently with

[3]The superscript and the subscript given with the expectation value define the range of the confidence interval.

TABLE III. s-wave average resonance parameters at S_n adopted in this work for the Pu isotopes and their energy dependence parameters above S_n. For comparison, $\bar{\Gamma}_\gamma^{l=0}$ values from the *Atlas of Neutron Resonances* [39] and from the RIPL-3 data base [26] are shown as well. Values with superscript $\diamond$, $\bullet$, $\triangleleft$, or $\star$ correspond, respectively, to our normalized model, the ENDF/B-VII evaluation, the best experimental assessment, or the best compromise for this isotope. Units are in meV except where otherwise stated.

CN Pu isotope	237	238	239	240	241	242	243	244	245
$\bar{\Gamma}_\gamma^{l=0}$ (Present)	$37.3^\diamond$	$41.3^\diamond$	$37.0^\diamond$	$39.0^\diamond$	$30.6^\bullet$	$36.0^\star$	$23.0^\triangleright$	$33.9^\diamond$	$20.3^\diamond$
$\bar{\Gamma}_\gamma^{l=0}$ (Atlas)	–	–	34 ± 3	43 ± 4	31 ± 2	36 ± 6	22 ± 1	–	20 ± 2
$\bar{\Gamma}_\gamma^{l=0}$ (RIPL-3)	–	–	34 ± 3	43 ± 4	31 ± 2	40.8 ± 4.6	23 ± 2	–	–
Θ [MeV]	2.4	3.89	4.5	3.99	3.25	3.70	4.8	3.1	3.7
$D_0[eV]$	4.5	0.2	9.6 ± 0.7	2.3 ± 0.1	13.7	0.8	15.5	1.2	17.

neutron-induced resonance cross-section data using AVXSF, will be the topic of a separate publication.

B. Fission transition states

1. Individual states

At low excitation energies above fundamental fission barriers, *ad hoc* sequences of individual transition states are postulated from the model described in Sec. III (see also Ref. [30]). Similarly, sequences of low-lying states are set up for the target nuclei from the literature (ENSDF database), augmented whenever needed by additional levels to complete the rotational bands predicted by our model. The consistency between input parameter and nuclear structure data was ensured among all Pu compound nuclear systems, for which the structures are especially dependent on their even-even or even-odd character.

2. Continuum level density

Approximately 1 MeV above the onset of each individual state sequence (corresponding to the energy where precise knowledge on the individual states fails), combinatorial quasiparticle-vibrational-rotational (QPVR) calculations were performed to construct LDs. Our QPVR procedure is fully consistent with the construction of the individual states because this is simply a generalization of the method used. The generalized model relies, in particular, on the neutron, Δ_n, and proton, Δ_p, pairing gaps [Eq. (41)] and the moments of inertia, $\hbar^2/(2\Im)$ [Eq. (43)]; all those parameters are possibly dependent on nucleus deformation and excitation energy. Strong considerations on those parameters are difficult to extract from neutron-induced cross-section experimental data fits alone, but the present work is aiming to marry theoretical and experimental information.

Nuclear structure calculations [25,32] indicate that the nucleus deviates from axial symmetry at the first saddle point, but recovers it at the outer saddle, where it exhibits mass-asymmetric shapes or higher order octuple deformations. Level densities are strongly dependent on broken symmetries at a particular point in configuration space and on nucleon pairing gaps.

Our QPVR model was primarily used as a support for constructing level densities at normal deformation, at which nucleon pairing gap parameters were adjusted to reproduce the observed slow neutron average resonance spacing values (listed in Table III). Figure 10 displays an example of total LD corresponding to the ground state with pairing gap values $\Delta_p = 0.81$ MeV, $\Delta_n = 0.74$ MeV for the fissioning ^{240}Pu nucleus. After some trial and error, it was decided to use our parametrized QPVR LD model for the inner barrier and an empirical pragmatic LD for the outer barrier [in the form of the multiphase-temperature model shown by Eq. (10)] whose parameters were tuned to reproduce reasonable experimental

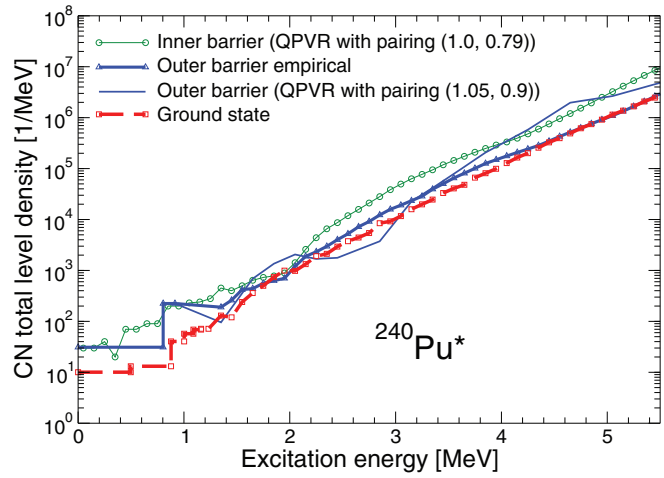

FIG. 10. (Color online) ^{240}Pu* total level densities as a function of excitation energy. The blue-triangled thick solid curve is our empirical outer barrier LD (15 constant temperature phases up to 7 MeV excitation energy) fitted to experimental cross sections, whereas the blue thin solid curve is based on our combinatorial model for the same density with pairing gap values ($\Delta_p = 1.05$ MeV, $\Delta_n = 0.9$ MeV). The green-dotted solid curve is our postulated inner barrier combinatorial LD (1.0, 0.79), superseded below 1.5 MeV by the specific inner individual transition state sequence.

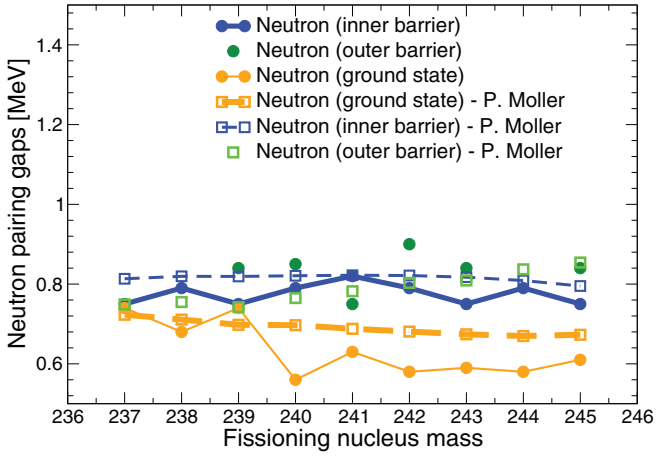

FIG. 11. (Color online) Present-work Pu neutron gaps (circles) plotted, respectively, at normal deformation (orange thin solid curve) and inner (blue thick solid line) and outer (green circles) barrier deformations. Theoretical values (open squares) by Möller [31] at normal deformation (orange thick dashed curve) and inner barrier deformation (blue thin dashed line) are displayed for comparison.

fission cross-section data and with, nonetheless, a strong support brought by a prior QPVR calculation. At the end, a value about 10% higher for the pairing energy parameters of the inner barrier relative to those of the normal deformation and 10% lower relative to those of the outer barrier has been found plausible on a nuclear surface dependence basis. This comes from the fact that the neutron and proton pairs, which participate actively in the pairing interaction, accumulate near the Fermi energy surfaces [33]. In addition, our pairing values tend to satisfy the common experimental observation [34] that in heavy nuclei the average proton pairing values tend to be higher than the neutron ones (Fig. 11 compared to Fig. 12). Finally, we can compare our estimated neutron and proton pairing gap parameters at ground-state and inner barrier

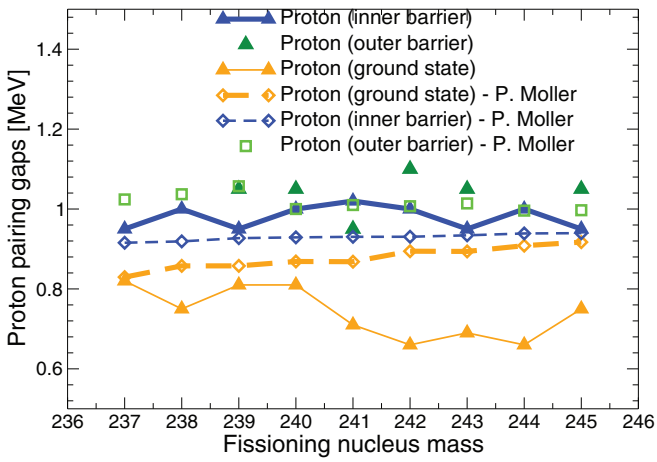

FIG. 12. (Color online) Present-work Pu proton gaps (triangles) plotted, respectively, at normal deformation (orange thin solid curve) and inner (blue thick solid line) and outer (green triangles) barrier deformations. Theoretical values (open diamonds) by Möller [31] at normal deformation (orange thick dashed curve) and inner barrier deformation (blue thin dashed line) are displayed for comparison.

deformation with the theoretical results from Möller *et al.* [31]. A general agreement over mass number is observed with the theoretical values as visible on Figs. 11 and 12 although at inner barrier deformation, our neutron pairing gaps are lower than the theoretical ones, whereas the opposite trend is noticed for the proton pairing gaps. The explanation comes from the fact that our neutron and proton pairing gaps were subordinated during the present LD fit; decorrelated adjustment of those quantities would have resulted in a very good agreement. At ground-state deformation, the systematic trend to be lower exhibited by our neutron and proton pairing gap parameters is simply attributable to actual renormalization on the observed slow neutron average resonance spacing data (D_0). At outer barrier deformation, no special comparison is made with the theoretical results from Möller *et al.* [31] because of our final choice of an adjusted multiphase-constant-temperature LD with no dedicated feedback on the pairing gap values.

3. *Multiphase-constant-temperature level density*

The use of a multiphase-constant-temperature LD for the outer barrier [Eq. (10)] can be justified by the following argument: Our present QPVR calculation performed at a given barrier deformation is representative of a frozen number of degrees of freedom in the excited nucleus (established quasiparticle, collective, and rotational spectrum configurations). No special credit is made for gradual or sudden shape changes of the deformed nucleus with increasing energy (tending towards sphericity) for which the nuclear temperature parameter might attest. Our fitted multiphase LD, $\rho(U, T)$, by using a constant but independent temperature T in each phase, can cope with this argument although other approaches exist to reproduce collective and rotational attenuations with increasing excitation energy (a blocking parameter for instance). No substantial investigations have been made in this issue during this work. However, use of temperature-dependent LD has been noticed in microscopic HFB calculations [35] but over a much larger excitation energy range (0–200 MeV).

4. *Semimicroscopic vs microscopic level densities*

Because reliable level densities are a crucial factor in any accurate determination of cross sections over any large energy range, it is interesting to compare our QPVR calculations with the HFB plus combinatorial method from Ref. [28].

Figures 13 and 14 show the level densities at ground state and at inner and outer barrier deformations obtained in the present study, respectively, for a fissile and a fertile isotope as well as with the HFB approach of Ref. [28] (which data are available from RIPL-3). The RIPL-3 second saddle LD contain by default the left-right asymmetry enhancement factor ($K_{\rm sym} \approx 2$), whereas the corresponding first saddle data do not contain any asymmetry enhancement factor for convenience. In our fit of the LD at the outer barrier, we have constrained the difference in collective enhancement (inner/outer ratio) within a range of 2–4, this ratio being judged acceptable on the following argument (quoting Ref. [36]): "If a saddle point exhibits a departure from axial symmetry with

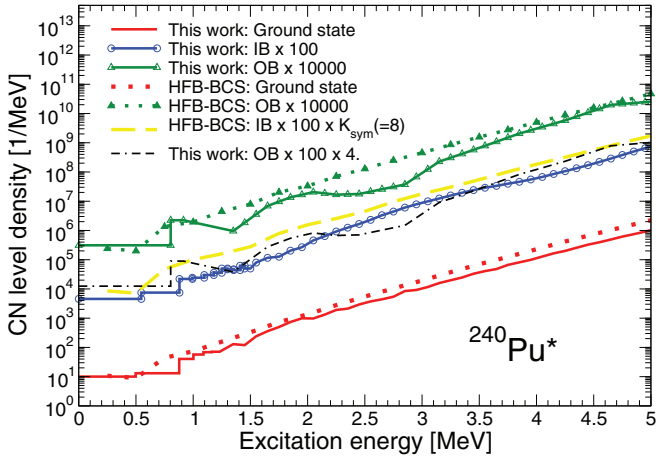

FIG. 13. (Color online) ^{240}Pu* total level densities as a function of excitation energy at ground state and, at inner and outer barrier deformations obtained in the present study and compared with HFB-BCS results [28]. Displayed LDs correspond, from bottom to top, to ground state and inner (multiplied by 100) and outer (multiplied by 10 000) barrier deformations. The wavy shape of our outer barrier multiphase temperature LD (15 constant temperature phases up to 7 MeV above fundamental barrier excitation energy, dash-dotted black curve) contrasts with our postulated inner barrier QPVR-BCS-type calculation (open-circle blue solid line); a maximum difference in collective enhancement factor of 4 is applied on the former for magnitude comparison.

preservation of D_2 symmetry relatively to the symmetry of the ground state, it implies an increase of a factor $\sqrt{(\pi/2)}\sigma_k$ and an additional factor 2 would result from a departure from reflection symmetry." For a direct comparison in terms of inner barrier LD, a maximum enhancement factor of 8 for axial symmetry breaking (triaxiality) with mirror symmetry was applied to the RIPL-3 first saddle data, which now look compatible with our calculated LD. This factor is also close to the values extracted from systematics on the Np family by Vladuca *et al.* [6].

From a general point of view, both LD shape and magnitude at ground state at inner barrier deformation are in good agreement. In terms of outer barrier LD, magnitudes are

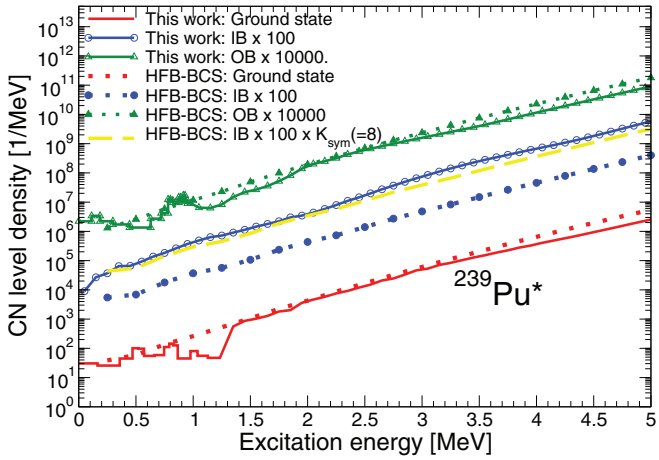

FIG. 14. (Color online) Same as Fig. 13, but for ^{239}Pu*.

similar, although the wavy shape of our combinatorial model LD departs from the monotonic slope of the RIPL-3 LD. From the considerations above and because pure microscopic HFB barriers are higher by a few hundred keV (with an increasing trend with mass number; see Figs. 8 and 9) than the present values (Table II), we can expect difficulties in providing reasonable fission cross sections from pure microscopic HFB for the Pu series. The authors of study [35] have logically obtained a significant agreement improvement by normalizing individually the prior microscopic barriers (prior fission cross section calculations were too low in magnitude) or an even better compatibility by fine tuning the LD, similar to the present approach, on both low-energy experimental target nucleus level schemes and neutron resonance spacing values at neutron threshold energy.

C. Total radiative capture widths

Prior estimates of total radiative capture widths, $\Gamma_\gamma^{J\pi}$, for each Pu isotope are obtained from

$$\bar{\Gamma}_\gamma^{J^\pi} = \frac{D_{J^\pi}}{2\pi}\int_0^E d\varepsilon_\gamma f(E,\varepsilon_\gamma)\sum_{J_f=|J-1|}^{J+1}\rho(E-\varepsilon_\gamma, J_f), \qquad (44)$$

where $f(E,\varepsilon_\gamma)$ contains the phase space factor $\varepsilon_\gamma^{(2L+1)}$ and radiation strength function for the multipolarity of the γ-ray transition while $\rho(E-\varepsilon_\gamma, J_f)$ is the LD of the states of the compound nucleus at excitation energy $(E-\varepsilon_\gamma)$.

We confine our model to $E1$ and $M1$ transitions on the grounds that electric quadrupole and higher multipolarity transitions contribute only very weakly to the overall neutron capture cross section. For the radiative strength function we use a modified version of the Kopecky-Uhl model [37]. For $E1$ transitions the strength function is

$$\frac{\Gamma_\gamma(E1)}{D\varepsilon_\gamma^3} = 0.418\times10^{-9}A^{2/3} + 4.62\times10^{-6}\frac{NZ}{N+Z} \times\sum_{k=1,2}\frac{k}{3}\frac{\Gamma_{Gk}(\varepsilon_\gamma)\varepsilon_\gamma}{\left[\left(\varepsilon_\gamma^2-E_{Gk}^2\right)^2+\varepsilon_\gamma^2\Gamma_{Gk}^2(\varepsilon_\gamma)\right]}, \qquad (45)$$

where $\Gamma_G(\varepsilon)=\Gamma_{G0}=\frac{B\varepsilon^2+C}{E_G^2}$.

The quantities $E_{G,k}$, $E_{G0,k}$ and B, C are input parameters for the model. In the present work we have used values for $E_{G,k}$, $E_{G0,k}$ that are close to the generally accepted parameters for the photonuclear giant resonance for the actinides, namely,

$$E_{G,1}=11\text{ MeV},\quad \Gamma_{G0,1}=2.9\text{ MeV},$$
$$E_{G,2}=14\text{ MeV},\quad \Gamma_{G0,2}=4.5\text{ MeV},$$
$$B=1,\quad C=10.$$

For $M1$ transitions the radiation strength function we use is

$$\frac{\Gamma_\gamma(M1)}{D\varepsilon_\gamma^3} = 0.237\times10^{-9}A^{1/3} + 0.536\times10^{-7}A^{1/3} \times\frac{\Gamma_{GM1}\varepsilon_\gamma}{\left[\left(\varepsilon_\gamma^2-E_{GM1}^2\right)^2+\varepsilon_\gamma^2\Gamma_{GM1}^2\right]}, \qquad (46)$$

with the parameters recommended in Ref. [37]; i.e., $E_{GM1}=6.6$ MeV and $\Gamma_{GM1}=4$ MeV.

The LD function that we use for the final states of the compound nucleus is calculated from our combinatorial QPVR model described in Sec. III. The pairing gap parameters are adjusted to give the neutron resonance spacing at the neutron separation energy. At the separation energy we join the combinatorial LD to a Fermi-gas form for the higher excitation energies; this conforms with the usage in our AVXSF code class I state densities of the compound nucleus.

Although the estimates for the coefficients in Eqs. (45) and (46) for the strength functions are mainly from theoretical considerations and the total radiation widths calculated in this way broadly agree (within 10% to 20%) with measured radiation widths, we have made a further empirical adjustment to them so that for $^{240}\mathrm{Pu} + n$ the calculation is in very close agreement with the radiation width measurement by Harvey *et al.* [38] at the 1.06-eV resonance; this appears to be the most accurate radiation width measurement available in the literature.

We have also used the above model to calculate radiation widths at energies well above the neutron separation energy. These exhibit a general increase in energy, which we have expressed approximately by applying an exponential factor to the value calculated at the separation energy, the "temperature" parameter in this factor being on the order of 3 MeV. This energy variation of the radiation width affects considerably the value of the radiative capture cross section at the higher neutron energies. Finally, we have taken into account the reduction of the capture cross section by the lower energy primary γ rays resulting in $(n, \gamma n')$ and $(n, \gamma f)$ branching.

Table III lists the s-wave average total radiation widths ($\bar{\Gamma}_\gamma^{l=0}$) and mean spacings ($D_0$) at neutron emission energy ($E = S_n$) used in this work. The radiation width, with no distinction of parity, is assumed to follow an exponential energy dependence $\bar{\Gamma}_\gamma^l(E) = \bar{\Gamma}_\gamma^l(S_n) \times e^{(E_n/\Theta)}$, whose parameters are quoted in Table III as well.

V. FISSION CROSS SECTIONS CALCULATED OVER A SUITE OF Pu ISOTOPES

We have compared our calculated cross sections to selected measurements or/and state-of-the-art evaluated libraries (e.g., ENDF/B-VII [40], JEFF-3.1.2 [41], and JENDL-4.0 [42]). In the case of the most important Pu isotopes (238–242), the evaluations are essentially based on experimental data where a plethora of direct (n, f) cross-section measurements exist.

The fission cross-section picture of the whole Pu family is well illustrated by sorting the isotopes as a function of their odd-even character. Figure 15 shows neutron-induced fission cross sections for the even Pu isotope targets, whereas Fig. 16 focuses on the odd Pu isotope targets. The first remark that we can make is about the generally good agreement between our results and the evaluated curves with the notable exception of the $^{243}\mathrm{Pu}(n, f)$ reaction. Standard fission-cross section evaluations include this isotope among the nonfissile nuclei, a fact invalidated by the present barrier height values, which are deduced from the $^{242}\mathrm{Pu}(t, pf)$ reaction and much

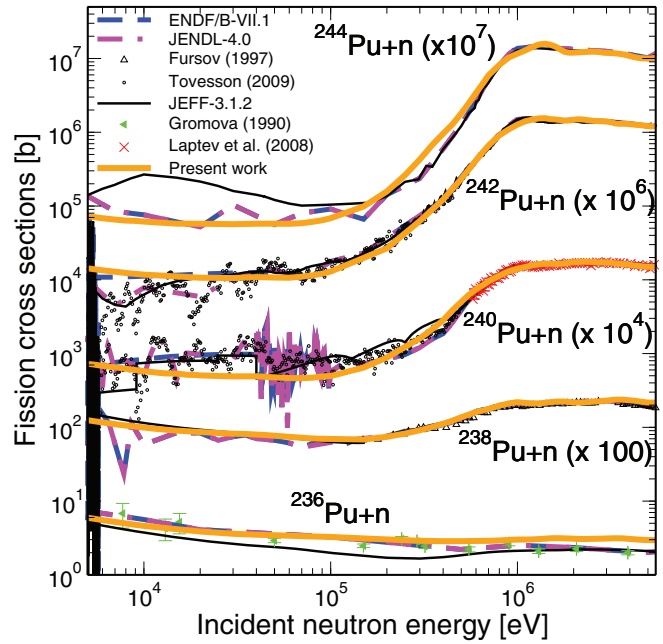

FIG. 15. (Color online) Overview of our calculated Pu fission cross sections versus neutron incident energy and masses (even isotope targets) compared to standard evaluated files (ENDF/B-VII.1 [40], JEFF-3.1.2 [41], and JENDL-4.0 [42]) and to recent measurements by Tovesson *et al.* [43], Laptev *et al.* [44], Fursov *et al.* [45], and Gromova *et al.* [46].

smaller than the neutron emission threshold (refer to ^{244}Pu* in Table II).

Additionally, we can make the following statements.

(i) The shape of the ^{236}Pu neutron-induced fission cross section is similar to that of a fissile nuclide on the basis of the barrier heights as determined from the analysis of the $^{237}\mathrm{Np}(^3\mathrm{He}, df)$ reaction. The values of these are both lower than the neutron emission threshold energy (Table II). Readers may refer to Appendix C to visualize the sensitivity to choice of barrier height parameters in the case of a fissile nuclide.

(ii) The $^{238}\mathrm{Pu}(n, f)$ reaction conserves partly the $^{236}\mathrm{Pu}(n, f)$ characteristic with an outer barrier height slightly below the neutron emission energy threshold, whereas the higher odd Pu fissioning systems are clearly pure nonfissile materials.

(iii) The pure nonfissile systems clearly manifest intermediate structures in their sub-threshold fission cross section and, depending on the energy resolution function of the apparatus and of their nature (class II compound states or incompletely damped vibrational class II states), might be partially or well resolved at low energy. Although smaller in magnitude relative to the fission cross-section level, experimental evidence of intermediate structures show up as well for the fissile isotopes (e.g., ^{240}Pu and ^{242}Pu* on Fig. 16).

(iv) The fit to the present ^{240}Pu neutron-induced fission cross section is satisfactory above 200 keV but our calculation is under-running a little bit below. Our

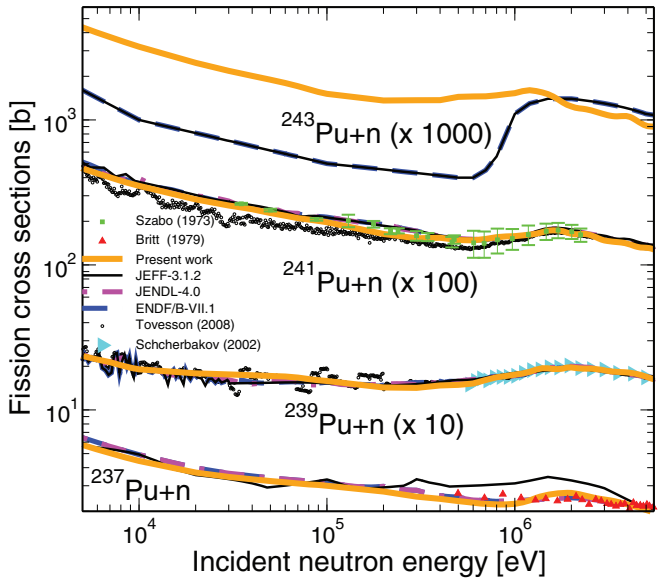

FIG. 16. (Color online) Overview of our calculated Pu fission cross sections as a function of neutron incident energy and masses (odd isotope targets) compared with the standard evaluated files (ENDF/B-VII.1, JEFF-3.1.2, and JENDL-4.0) and the recent measurements performed by Tovesson *et al.* [49] and Shcherbakov *et al.* [51]. The ^{237}Np(^{3}He,df)^{238}Pu* fission probability measurement from Back *et al.* [52], transposed in terms of fission cross section, is the unique experimental data support for the (^{237}Pu + n) system.

subthreshold fission calculation ($V_A = S_n + 670$ keV> $V_B = S_n + 430$ keV) is strongly conditioned to the specific inner barrier transition state tunneling factor and particularly on the Nilsson single-neutron quasiparticle state sequence we use in combination with the zero- and one-γ vibrations. We keep in mind that we do calculate an *average* fission cross section and no special provision has been made in the present work to reproduce the observed fluctuations, possibly owing to incompletely damped class II vibrational resonances. Among the evaluated files displayed with our (^{240}Pu + n) simulation, none rely on strong theoretical support. JENDL-4.0 results from a fine average of genuine experimental data, JEFF-3.1.2 uses a pragmatic steplike function (in three groups) based on integral data feedback [47] in the [5.7–40]-keV unresolved resonance energy range (URR), whereas ENDF/B-VII.1 is based on a standard Hauser-Fesbach average cross-section calculation in the URR domain. Between 40 and 550 keV, the ENDF/B-VII.1 fission cross section borrows the JENDL-4.0 evaluation.

(v) A notable departure from the overall trend with mass number of the odd-mass target fission cross sections is that of ^{239}Pu, which shows a considerably lower value at low neutron energies than the others. This illustrates the influence of the individual transition states within the energy gap at the barrier deformations. ^{239}Pu has spin and parity $J^{\pi} = 1/2^{+}$, implying that s-wave neutrons form the compound nucleus in 0^{+} and 1^{+} states, the latter being predominant. There is no single or combined vibrational mode that will provide a low-energy transition state with $J^{\pi} = 1/2^{+}$; the most obvious candidate for such a state at the outer barrier is the combination of the mass-asymmetry mode ($K^{\pi} = 0^{-}$) with a bending vibration ($K^{\pi} = 1^{-}$). This is also a candidate (at higher energy) for the inner barrier, but another possible candidate is a two-quasiparticle state above the energy gap. In our calculations physically reasonable values are assigned to these transition states and succeed in explaining the comparatively low value of the low-energy fission cross section of ^{239}Pu (see also Ref. [48]).

(vi) Our computed ^{241}Pu neutron-induced fission cross section lies between the two measurements by Tovesson *et al.* [49] and Szabo *et al.* [50]. The high-precision data from Tovesson *et al.* [49], although resulting from a well-tested technique, are 20%–30% lower than the standard evaluations and need to be confirmed.

VI. RESULTS ON CAPTURE CROSS SECTIONS

Because our work is supported by the commonly admitted GDR (based on Fermi-liquid theory) model of the total capture width whose constants have been carefully adjusted in this study to the most accurate radiation width measurement available over the range of the Pu isotope series (see Sec. IV C), it is opportune to gauge the accuracy of our calculations in terms of capture cross section. The ^{239}Pu and ^{240}Pu neutron-induced capture cross sections are the most suitable candidates for that comparison because sound experimental data do exist, the information from which is well represented by the most commonly used evaluated files.

Figure 17 shows our calculated ^{240}Pu neutron-induced capture cross section compared to the best capture measurement by Weston and Todd [53]. The authors claim an accuracy

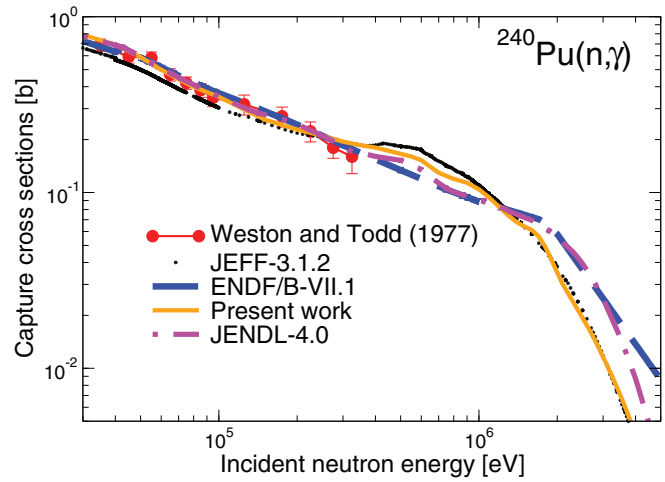

FIG. 17. (Color online) ^{240}Pu neutron-induced capture cross section (orange solid curve) computed with AVXSF and compared with evaluated data (ENDF/B-VII.1, JEFF-3.1.2, and JENDL-4.0) and the most accurate capture measurement by Weston and Todd [53].

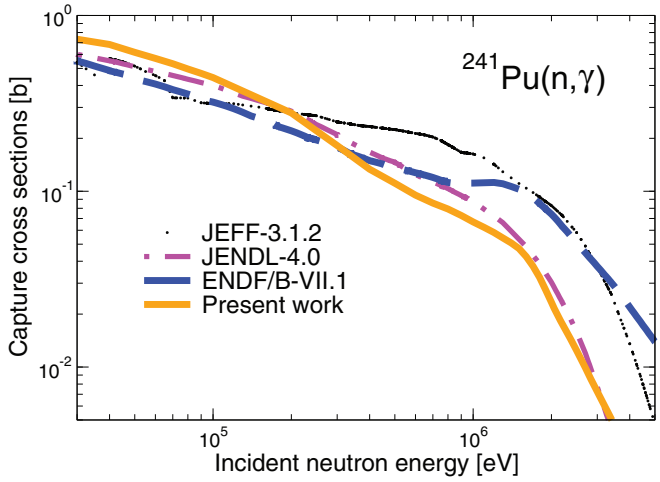

FIG. 18. (Color online) ^{239}Pu capture cross section (orange solid curve) computed with AVXSF and compared to some evaluated data (ENDF/B-VII.1, JEFF-3.1.2, and JENDL-4.0) and the old measurement by Hopkins *et al*. [55].

of 7% at the lower edge energy (250 eV), reaching 20% at the upper edge (325 keV). The agreement of the present calculation is satisfactory with this experimental data set, which is also used as reference for the ENDF/B-VII.1 and JENDL-4.0 evaluations. It is apparent from Fig. 17 that the JEFF-3.1.2 curve is significantly lower than Weston and Todd [53] data (precisely by a factor −12%). However, an average capture width of (30.7 ± 2.5) meV is quoted by the author of study [47], a study which, in addition to condensing the information from the whole resonance range, is the foundation of the JEFF-3.1.2 evaluation at low energy ($E_n < 40$ keV). This value consolidates the choice we have made for the normalization of our total capture width prediction model but also advocates a renormalization of the Weston and Todd [53] capture measurement (possibly between −3% and −5%). Above 1 MeV, we observe strong differences between evaluated radiative capture cross sections because of the lack of experimental data. This fact is well identified in Ref. [54], whose authors also emphasize the weakness of the fission models in standard average cross-section codes.

Another valuable comparison can be conducted on the ^{239}Pu neutron capture cross section (see Fig. 18). The experimental database above the resonance range is rather poor and we must rely on the unique and old average measurement by Hopkins *et al*. [55]. We observe that the evaluations differ significantly above 700 keV, where no experimental data are available and where the very small value of the capture cross section complicates any measurement. The present AVXSF calculation deviates from the smooth compound nucleus formation shape at about 1.5 MeV. The investigation of this Wigner-cusp-type inflection shows that this is attributable to the strong competition by other open channels. From this observation, we do realize the importance of relying on sound theoretical grounds for the best possible treatment of the inelastic and fission competitive cross sections.

VII. CROSS-SECTION PREDICTION CAPABILITY OVER THE COMPOUND NUCLEUS ENERGY RANGE

The consistent approach, carried out all the way during this work and on the suite of the Pu isotopes, gives us the opportunity to interpolate or extrapolate barrier parameters to the poorly known nuclei of that series with some reliability. Because of the total lack of neutron-induced experimental data, a prediction on the average fission cross section of the very short-lived ^{243}Pu ($\tau_{1/2} = 4.95$ h) is a suitable example of application of the methodology developed. However, the existence of a surrogate measurement, the ^{242}Pu(t, pf) reaction from Back *et al*. [52] brings some support for choosing representative barrier heights but the robustness of the prediction is mainly ensured by the models and trends used in the cross section study of the other Pu isotopes (in particular on the information derived from the ^{243}Pu* excited nucleus and the ^{244}Pu residual nucleus level densities involved, respectively, in the analyses of the neutron-induced ^{242}Pu and ^{244}Pu cross sections). We observe in Fig. 19 that our predicted average *subthreshold* fission cross section is about twice the ENDF/B-VII.1 (≡JEFF-3.1.2) evaluated cross section. This well demonstrates that the ^{243}Pu target isotope is a fissile nucleus with estimated inner and outer barrier heights of 5.30 and 5.25 MeV, respectively, significantly lower than the neutron emission threshold (6.02 MeV). Contrary to the fission reaction, no conflicting trends with the ENDF/B-VII.1 (JEFF-3.1.2) evaluations are found in terms of capture or inelastic cross sections, confirming that the origin of the differences is essentially attributable to the choice of different barrier heights. Both evaluated files (ENDF/B-VII.1, JEFF-3.1.2) rely

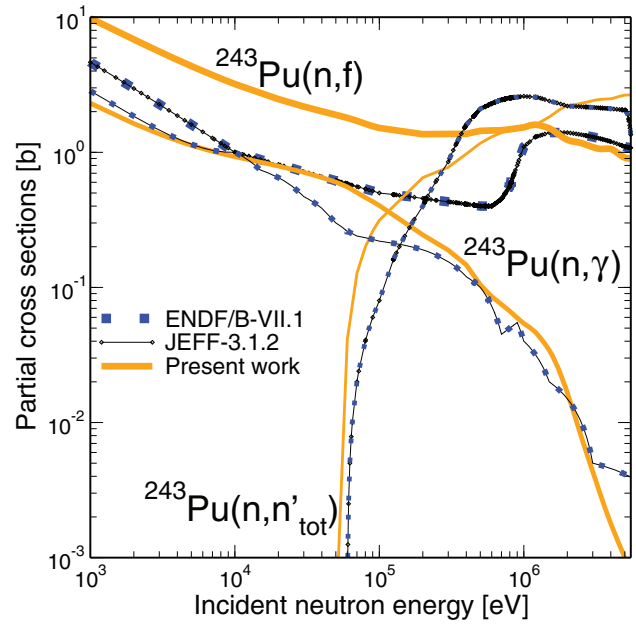

FIG. 19. (Color online) ^{243}Pu partial cross sections (orange solid curves) computed with AVXSF and compared to the ENDF/B-VII.1 (blue dotted curves) and JEFF-3.1.2 (black solid curves with circles) evaluated data. No recommendation is found in the JENDL-4.0 data library for this isotope. Thick, medium-thick, and thin curves correspond, respectively, to the (n, f), (n, γ), and (n, n'_{tot}) reactions.

on the old Howerton-MacGregor evaluation (1975) [56], which included very poor experimental information (three fission cross-section data points above the fission threshold (from 1.5 to 2 MeV) and a few spectrum-averaged fission and capture data points). Ultimately, Howerton-MacGregor complemented their evaluation in terms of fission cross section at the higher energies from systematics.

VIII. CONCLUSIONS AND FUTURE ORIENTATIONS

The *R*-matrix theory applied to the modeling of fission cross sections was developed in the early 1970s and carefully used to interpret specific experimental cases of intermediate structure until the end of the 1980s. However, this is the first time that this theory has been used methodically and consistently for a whole isotope family (plutonium) over a broad energy range, from the upper end of the resolved resonances to the onset of second chance fission. In addition, a direct Monte Carlo sampling of class I and class II state parameters for *R*-matrix calculations of double-hump barrier resonance effects is performed and supersedes the assumption of decoupled class II fluctuation correction factor and analytical sub-barrier average probability. This leads to a significantly improved partial cross section accuracy with, in particular, a correction of up to 20% of the usual calculated average fission cross section.

Another significant improvement on the agreement between experimental and simulated fission cross sections is achieved by assigning fined-tuned quasiparticle-vibrational sequences of individual transition-state bandheads, the impact of which is quite sizable at low excitation energies (relative to the fission barriers). At higher energies our robust semimicroscopic combinatorial LD as a function of deformation provides the desired strong physics background to give cross-section simulations of quality comparable with current evaluations. Although in our current analysis scheme it is still necessary to fit the outer barrier LD, we can show that the fit is semiquantitatively describable by our semimicroscopic formulation. Furthermore, the energy gap parameters necessary for these level densities increase systematically with nuclear deformation, and this increase can explain the odd-even staggering of barrier heights relative to the ground state.

By applying this approach consistently through a long series of plutonium isotopes, possible deficiencies in modern evaluated libraries can be identified. Finally, we show that extrapolated or interpolated barrier heights and level densities can be used to make reliable cross-section predictions for the short-lived isotopes of the series. As far as the ^{244}Pu* excited nucleus is concerned, our predicted neutron-induced fission cross section is twice the value of the ENDF/B-VII.1 and JEFF-3.1.2 evaluations in the low-energy range and therefore suggests a revision of those files because it has been obtained in a quite consistent approach between all Pu isotopes.

The collaboration work summarized in this article will eventually be integrated in the validated routes and/or modern code structures such as CONRAD [57] at CEA Cadarache and GNASH [58] and COH [59] at LANL. It might also supply additional pieces of information in the framework of the new CIELO [60] international effort on current standard evaluated data libraries.

Ongoing developments in the AVXSF code will continue to refine class I and class II state coupling models. The latter objective will require consideration of the *S*-matrix formulation of the collision matrix, rather than the *R*-matrix form, but only in very special coupling situations. Another effect will focus on the consistent treatment of transfer as well as photon-induced fission reactions in addition to the more common (n, f) reactions.

ACKNOWLEDGMENTS

We are indebted to Peter Möller (LANL) for the many fruitful discussions about his macroscopic-microscopic model and especially for provisioning the associated data material. One of the authors (O. Bouland) expresses his deep gratitude to the T-2 group of LANL for hosting and funding complement during the years 2009–2010. The LANL contribution was performed under the auspices of the U.S. Department of Energy by Los Alamos National Security, LLC, under Contract No. DE-AC52-06NA25396.

APPENDIX A: LEVEL SPACING DISTRIBUTIONS

The direct Monte Carlo technique adopted in this study relies, in particular, on class I and class II eigenstate energy selection from relevant level spacing statistical distributions with suitable averages. Because the number of class II levels involved in a trial calculation is much smaller than the number of class I levels ($D_{\mathrm{I}} \approx 50 \times D_{\mathrm{II}}$ about S_n), we can diagonalize "on line" the corresponding matrices to determine a plausible sequence of class II eigenvalues. However, to reduce the amount of computational effort, we use "quintaxial" matrices, in which all the elements are zero except those on the diagonal axis and the two adjacent axes on either side of the diagonal. The diagonal elements are drawn from a poisson distribution and the nonzero nondiagonal elements from a Gaussian distribution with zero mean and dispersion value that is equal to the square of the mean of the Poisson distribution. We find that these "quintaxial" matrices result in both satisfactory first-neighbor spacing distributions and long-range correlations. Figure 20 shows an example of class II level spacing distribution (blue thin histogram) constructed from our hypotheses.

The amount of computer time required to diagonalize the large matrix involved for a class I sequence in each trial of a Monte Carlo process would be prohibitively large. Therefore, we use a separately computed file of a large eigenvalue sequence. This has the properties of a first-neighbor spacing distribution that is similar to the Wigner form [61] and has long-range correlations that approximate closely to the Dyson-Mehta Δ statistic [62]. This *ad hoc* class I spacing distribution is also plotted on Fig. 20 (red thick histogram) and compared to the standard Wigner law (dashed curve). The choice to use the same class I energy sequence for every trial can be justified by locating randomly the "medium-energy"

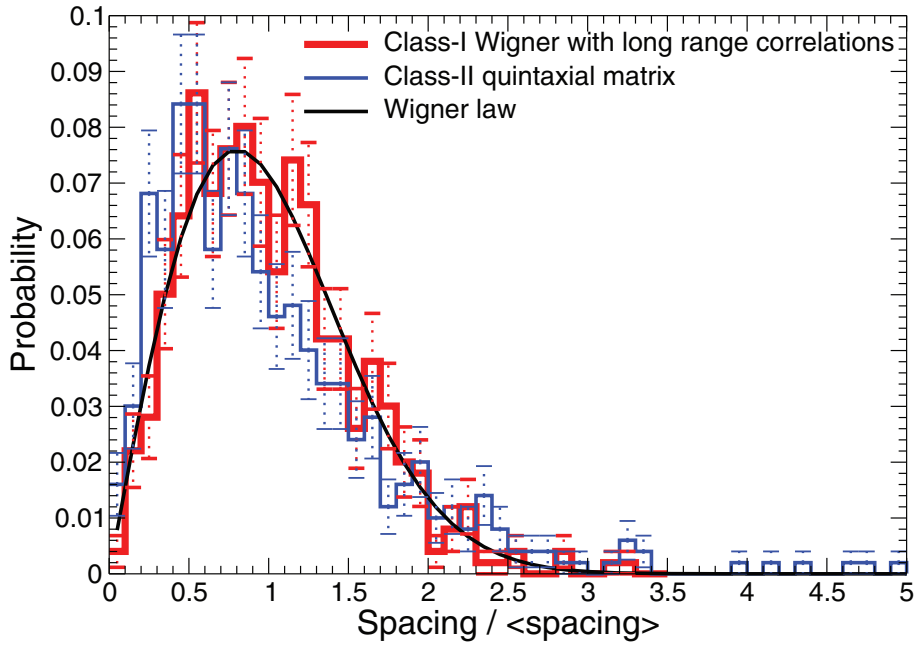

FIG. 20. (Color online) Class I level spacing distribution (red thick histogram) obtained from a simulation of 500 eigenvalues and ruled by a Wigner law amended with long-range correlations. A plausible class II distribution (blue thin histogram) based on a quintaxial matrix diagonalization of the same number of eigenvalues is shown as well for comparison. The pure Wigner law (black solid curve) is displayed as a reference. Uncertainties associated with drawing statistics are also plotted (vertical bars).

class II state within this sequence and therefore "watching" a different pattern of class I states in every trial.

Differences observed on plotted level spacing distributions suggest a possible impact on the resulting Monte Carlo average fission cross section value although the average over numerous direct Monte Carlo calculations will likely wash out these very small deviations which, at the end of the day, will be of a magnitude comparable to or even smaller than the background contribution of the "distant class II states" (see Appendix B).

APPENDIX B: DISTANT CLASS II BACKGROUND EFFECT

Far away from the medium-energy class II level selected, the contribution of the most distant class II compound states [other than the neighboring class II states already considered in Eqs. (36) and (37)] might also be significant. From a general point of view, the reduced-width amplitude of final R-matrix eigenstates in a reaction channel c can be split into four components,

$$\gamma_{\lambda_i,c} = C_{\lambda_i(\lambda_{\mathrm{II}_{\mathrm{medium}}})}\gamma_{\lambda_{\mathrm{II}_{\mathrm{medium}}},c} + \sum_{\lambda_{\mathrm{I}}} C_{\lambda_i(\lambda_{\mathrm{I}})}\gamma_{\lambda_{\mathrm{I}},c} + \sum_{\lambda_{\mathrm{II}_{\mathrm{neighbors}}}} C_{\lambda_i(\lambda_{\mathrm{II}})}\gamma_{\lambda_{\mathrm{II}},c} + \sum_{\lambda_{\mathrm{II}_{\mathrm{distant}}}} C_{\lambda_i(\lambda_{\mathrm{II}})}\gamma_{\lambda_{\mathrm{II}},c}. \quad \text{(B1)}$$

The fourth component of the right-hand side in Eq. (B1) acts as a background term and can be expressed using perturbation theory such that

$$\sum_{\lambda_{\mathrm{II}_{\mathrm{distant}}}} C_{\lambda_i(\lambda_{\mathrm{II}})}\gamma_{\lambda_{\mathrm{II}},c} \approx \sum_{\lambda_{\mathrm{II}_{\mathrm{distant}}}} \frac{\langle\lambda_{\mathrm{I}}|H_c|\lambda_{\mathrm{II}}\rangle}{\left(E_{\lambda_{\mathrm{II}}} - E_{\lambda_{\mathrm{I}}}\right)}\gamma_{\lambda_{\mathrm{II}},c}. \quad \text{(B2)}$$

In particular, the sum of the squares of the distant class II state contributions [right-hand side in Eq. (B2)] to a quasi-class I radiative capture reduced width, under the assumption of no correlations in sign among matrix elements, can be approximated as

$$\sum_{\lambda_{\mathrm{II}_{\mathrm{distant}}}} \frac{\langle\langle\lambda_{\mathrm{I}}|H_c|\lambda_{\mathrm{II}}\rangle^2\rangle}{\left(E_{\lambda_{\mathrm{II}}} - E_{\lambda_{\mathrm{I}}}\right)}\left\langle\gamma^2_{\lambda_{\mathrm{II}},\gamma}\right\rangle \approx \left\{\left|\frac{1}{\sin^2(\pi x)} - \frac{1}{\pi^2}\left[\frac{1}{x^2} + \sum_{j=1}^{N_{\lambda_{\mathrm{II}}}}\left(\frac{1}{(j-x)^2} + \frac{1}{(j+x)^2}\right)\right]\right|\right\} \times \frac{\pi}{2}\frac{D_{\mathrm{I}}}{D^2_{\mathrm{II}}}\bar{\Gamma}_{\lambda_{\mathrm{II}\downarrow}}\bar{\Gamma}_{\lambda_{\mathrm{II}},\gamma}, \quad \text{(B3)}$$

with $x = \dfrac{\varepsilon_{\lambda_i} - E}{D_{\mathrm{II}}}$ and E the incident particle energy.

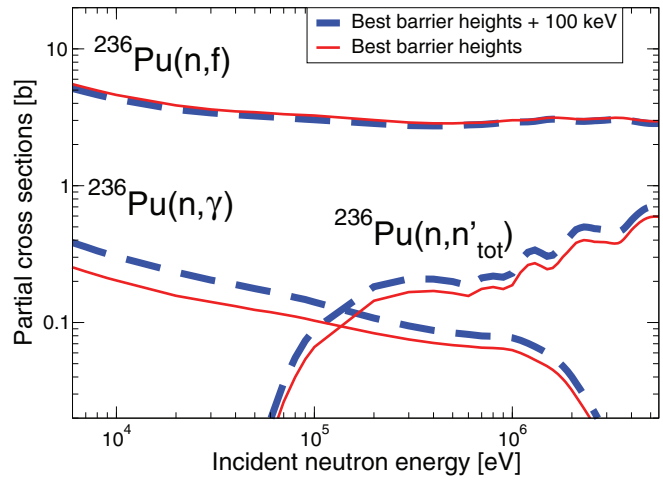

FIG. 21. (Color online) ^{236}Pu fission, inelastic, and capture cross sections computed with our AVXSF code. The red solid curves have been established using inner and outer barrier heights, respectively, equal to 5.6 and 4.95 MeV, whereas the blue dashed curves correspond to the same barriers but increased by 100 keV.

Because any partial fission width over a single Bohr transition channel (μ) is assumed to follow a Porter-Thomas distribution with one degree of freedom only, the assumption of no correlation between reduced-width amplitudes in sign does not hold for fission and the result from Eq. (B3) is used as standard deviation for drawing from a zero-mean Gaussian distribution the amount and the sign of the background term to be added to the previously calculated reduced fission width amplitude of the quasi-class I eigenstates [Eq. (29) or (37)].

APPENDIX C: EXAMPLE OF SENSITIVITY TO CHOICE OF BARRIER HEIGHT PARAMETERS

Figure 21 shows the fission, inelastic, and capture neutron-induced cross sections of ^{236}Pu. An increase by 100 keV on the barrier heights has a major impact on the predicted capture and inelastic cross sections, whereas no comparable change is encountered on the corresponding fission cross section. That pattern is characteristic of fissile isotopes whose barrier heights lie below the neutron emission threshold (respectively, 260 and 910 keV below S_n at barriers A and B in the ^{237}Pu* system), by contrast with a fertile isotope for which neutron-induced fission cross-section sensitivity is large with barrier height.

[1] S. R. Lesher, J. T. Burke, L. A. Bernstein, H. Ai, C. W. Beausang, D. L. Bleuel, R. M. Clark, F. S. Dietrich, J. E. Escher, and P. Fallon, Phys. Rev. C **79**, 044609 (2009).

[2] B. Jurado, G. Kessedjian, M. Petit, M. Ache, G. Barreau, A. Bidaud, S. Boyer, N. Carjan, S. Czajkowski, and D. Dassie, Eur. Phys. J. **2**, 06004 (2010).

[3] S. Bjørnholm and J. E. Lynn, Rev. Mod. Phys. **52**, 725 (1980).

[4] M. J. López Jiménez, B. Morillon, and P. Romain, Ann. Nucl. Energy **32**, 195 (2005).

[5] M. Sin, R. Capote, A. Ventura, M. Herman, and P. Obložinský, Phys. Rev. C **74**, 014608 (2006).

[6] G. Valduca, A. Tudora, B. Morillon, and D. Filipescu, Nucl. Phys. A **767**, 112 (2006).

[7] J. E. Lynn, Nuclear Physics Division, **AERE, Harwell - R 7468-PS/HL74/4382(C17)** (1974).

[8] W. Hauser and H. Feshbach, Phys. Rev. **87**, 366 (1952).

[9] P. A. Moldauer, Phys. Rev. **123**, 968 (1961).

[10] L. Dresner, Columbia University Report No. CU-175 (1957), p. 71.

[11] S. Hilaire, Ch. Lagrange, and A. J. Koning, Ann. Phys. **306**, 209 (2003).

[12] V. M. Strutinsky, Nucl. Phys. A **95**, 420 (1967).

[13] J. E. Lynn, J. Phys. A: Math. Nucl. Gen. **6**, 542 (1973).

[14] S. Bjørnholm and V. M. Strutinsky, Nucl. Phys. A **136**, 1 (1969).

[15] D. L. Hill and J. A. Wheeler, Phys. Rev. **89**, 1102 (1953).

[16] J. E. Lynn and B. B. Back, J. Phys. A: Math. Nucl. Gen. **7**, 395 (1974).

[17] H. Weigmann, in *The Nuclear Fission Process*, edited by C. Wagemans (CRC Press, Boca Raton, FL, 1991), p. 7.

[18] C. E. Porter and R. G. Thomas, Phys. Rev. **104**, 483 (1956).

[19] T. Papenbrock and H. A. Weidenmüller, Rev. Mod. Phys. **79**, 997 (2007).

[20] A. Gilbert and A. G. W. Cameron, Can. J. Phys. **43**, 1446 (1965).

[21] H. Uhrenholt, S. Åberg, P. Möller, and T. Ichikawa, arXiv:0901.1087v2.

[22] D. J. Rowe, *Nuclear Collective Motion—Models and Theory* (Methuen, London, 1970).

[23] C. Gustafson, I. L. Lamm, B. Nilsson, and S. G. Nilsson, Ark. Fys. **36**, 613 (1967).

[24] A. Bohr and B. R. Mottelson, Phys. Rev. **90**, 717 (1953).

[25] P. Möller, A. J. Sierk, T. Ichikawa, A. Iwamoto, R. Bengtsson, H. Uhrenholt, and S. Åberg, Phys. Rev. C **79**, 064304 (2009).

[26] R. Capote, M. Herman, P. Obložinský, P. G. Young, S. Goriely, T. Belgya, A. V. Ignatyuk, A. J. Koning, S. Hilaire, and V. A. Plujko, Nucl. Data Sheets **110**, 3107 (2009).

[27] G. N. Smirenkin, IAEA Report No. INDC(CCP)-359, 1993.

[28] S. Goriely, S. Hilaire, A. J. Koning, M. Sin, and R. Capote, Phys. Rev. C **79**, 024612 (2009).

[29] G. F. Auchampauch and L. Weston, Phys. Rev. C **12**, 1850 (1975).

[30] O. Bouland, J. E. Lynn, and P. Talou, Eur. Phys. J. **2**, 08001 (2010).

[31] P. Möller (private communication at LANL).

[32] J.-P. Delaroche, M. Girod, H. Goutte, and J. Libert, Nucl. Phys. A **771**, 103 (2006).

[33] D. G. Madland and J. R. Nix, Nucl. Phys. A **476**, 1 (1988).

[34] A. Bohr and B. R. Mottelson, in *Nuclear Structure*, Vol. 1 (Benjamin, New York, 1969), p. 302.

[35] S. Hilaire, S. Goriely, M. Girod, A. J. Koning, R. Capote, and M. Sin, Eur. Phys. J. **2**, 04005 (2010).

[36] S. Bjørnholm, A. Bohr, and B. R. Mottelson, IAEA Report No. IAEA-SM-174/205 (1973), Vol. 1, p. 367.

[37] J. Kopecky and M. Uhl, Phys. Rev. C **41**, 1941 (1990).

[38] J. A. Harvey, H. A. Mook, N. W. Hill, and O. Shahal, in *Proceedings of the International Conference on Nuclear Data for Science and Technology, Antwerp, Belgium*, edited by K. H. Bockhoff (D. Reidel, Dordrecht, 1982), p. 961.

[39] S. F. Mughabghab, *Atlas of Neutron Resonances*, 5th ed. (Elsevier, Amsterdam, 2006).

[40] M. B. Chadwick, P. Obložinský, M. Herman, N. M. Greene, R. D. McKnight, D. L. Smith, P. G. Young, R. E. MacFarlane, G. M. Hale, and S. C. Frankle, Nucl. Data Sheets **107**, 2931 (2006).

[41] A. Santamarina, D. Bernard, P. Blaise, M. Coste, A. Courcelle, T. D. Huynh, C. Jouanne, P. Leconte, O. Litaize, S. Mengelle, and G. Noguère, JEFF Report No. 22, 2009, edited by A. Santamarina, OECD/NEA.

[42] K. Shibata, O. Iwamato, T. Nakagawa, N. Iwamoto, A. Ichihara, S. Kunieda, S. Chiba, K. Furutaka, N. Otuka, and T. Ohasawa, J. Nucl. Sci. Technol. **48**, 1 (2011).

[43] F. Tovesson, T. S. Hill, M. Mocko, J. D. Baker, and C. A. McGrath, Phys. Rev. C **79**, 014613 (2009).

[44] A. B. Laptev, O. A. Shcherbakov, A. S. Vorobyev, R. C. Haight, and A. D. Carlson, in *Proceedings of the Fourth International Conference on Fission and Properties of Neutron-Rich Nuclei, Sanibel Island, FL, USA, 2007* (World Scientific, Singapore, 2008), p. 462.

[45] B. I. Fursov, V. N. Polynov, B. F. Samylin, and V. S. Shorin, in *Proceedings of the 3rd International Conference on Nuclear Data for Science and Technology, Trieste, Italy*, edited by G. Reffo, A. Ventura, and C. Grandi, Vol. 59 (Italian Phys. Soc., Bologna, 1997), p. 488.

[46] E. F. Gromova, S. S. Kovalenko, Yu. A. Selitskiy, A. M. Frldkin, V. B. Funshteyn, V. A. Yakovlev, S. V. Antipov, P. E. Vorotnlkov, B. M. Gokhberg, and V. V. Danichev, Sov. At. Energy **68**, 223 (1990).
[47] O. Bouland, *Re-evaluation of the* ^{240}Pu *Cross Sections in the Unresolved Resonance Energy Range* (JEFDOC-917 NEA/OECD Paris Publications, Paris, 2002).
[48] J. E. Lynn and A. C. Hayes, Phys. Rev. C **67**, 014607 (2003).
[49] F. Tovesson and T. S. Hill, Nucl. Sci. Eng. **165**, 224 (2010).
[50] I. Szabo, J. L. Lerot, and J. P. Marquette, Proc. Conf. Neutron Phys., Kiev 1973, **3**, 27 (1974).
[51] O. A. Shcherbakov, A. B. Laptev, G. A. Petrov, A. S. Vorobyev, A. V. Fomichev, A. Y. Donets, A. V. Evdokimov, S. M. Soloviev, Y. V. Tuboltsev, and T. Fukahori, in *Proceedings of International Conference on Fission and Properties of Neutron-Rich Nuclei, Sanibel Island, FL, USA 2002* (World Scientific, Singapore, 2003), p. 515.
[52] B. B. Back, O. Hansen, H. C. Britt, and J. D. Garrett, Phys. Rev. C **9**, 1924 (1974).
[53] L. W. Weston and J. H. Todd, Nucl. Sci. Eng. **63**, 143 (1977).
[54] P. Talou, P. G. Young, T. Kawano, M. Rising, and M. B. Chadwick, Nucl. Data Sheets **112**, 3054 (2011).
[55] J. C. Hopkins and B. C. Diven, Nucl. Sci. Eng. **12**, 169 (1962).
[56] R. J. Howerton and M. H. MacGregor, Lawrence Livermore National Laboratory Report No. UCRL-50490 (1978), 15, Part D, Rev. 1, pp. 379–384.
[57] C. De Saint Jean, B. Habert, O. Litaize, G. Noguère, and C. Suteau, in *Proceedings of the International Conference on Nuclear Data for Science and Technology, Nice France, 2007* (EDP Science, Les Ulis Cedex, France, 2008), p. 251.
[58] P. G. Young, E. D. Arthur, and M. B. Chadwick, Los Alamos National Laboratory Technical Report No. LA-12343-MS, 1992.
[59] T. Kawano, P. Talou, M. B. Chadwick, and T. Watanabe, J. Nucl. Sci. Technol. **47**, 462 (2010).
[60] M. B. Chadwick, *CIELO: Collaborative International Evaluation Library Organization: Rationale, Progress, and Plans* (NEA/OECD Paris Publications, Paris, 2012), JEFDOC-1457.
[61] E. P. Wigner, Technical Report ORNL-2309, 59 (1956).
[62] F. J. Dyson and M. L. Mehta, J. Math. Phys. **4**, 701 (1963).